

Soft Matter

rsc.li/soft-matter-journal



ISSN 1744-6848

PAPER

Gareth H. McKinley *et al.*
Elastoviscoplasticity, hyperaging, and
time-age-time-temperature superposition
in aqueous dispersions of bentonite clay



Cite this: *Soft Matter*, 2023,
19, 7293

Elastoviscoplasticity, hyperaging, and time–age–time–temperature superposition in aqueous dispersions of bentonite clay†

Joshua David John Rathinaraj, ‡^a Kyle R. Lennon, ‡^b Miguel Gonzalez, ^c Ashok Santra, ^c James W. Swan^b and Gareth H. McKinley *^a

Clay slurries are both ubiquitous and essential in the oil exploration industry, and are most commonly employed as drilling fluids. Due to its natural abundance, bentonite clay is often the *de facto* choice for these materials. Understanding and predicting the mechanical response of these fluids is critical for safe and efficient drilling operations. However, rheological modeling of bentonite clay suspensions is complicated by the fact that thermally-driven microscopic arrangements of particle aggregates lead to a continual evolution of the viscoelastic properties and the yield stress of the suspension with time. Ergodic relations fundamental to linear viscoelastic theory, such as the Boltzmann superposition principle, do not hold in this scenario of 'rheological aging'. We present an approach for modeling the linear viscoelastic response of aging bentonite suspensions across a range of temperatures that is based on the transformation from laboratory time to an effective 'material time' domain in which time-translation invariance holds, and the typical relations of non-aging linear viscoelastic theory apply. In particular, we model the constitutive relationship between stress and strain-rate in the bentonite suspensions as fractional Maxwell gels with constant relaxation dynamics in the material time domain, in parallel with a non-aging Newtonian viscous contribution to the total stress. This approach is supported by experimental measurements of the stress relaxation and rapid time-resolved measurements of the linear viscoelastic properties performed using optimized exponential chirps. This data is then reduced to master curves in the material domain using time–age–time superposition to obtain best fits of the model parameters over a range of operating temperatures.

Received 12th April 2023,
Accepted 2nd August 2023

DOI: 10.1039/d3sm00492a

rsc.li/soft-matter-journal

1 Introduction

Aqueous dispersions of discotic clay platelets exhibit a number of mechanical properties that are of great interest to certain commercial applications, perhaps most notably to drilling operations in the oil and gas industry^{1–8} where these dispersions are pumped into boreholes and serve a number of purposes including the removal of rock cuttings produced in the drilling process.^{7,9} The essential thermo-rheo-mechanical properties of the dispersion in such applications include the rapid development of a yield stress – which allows the

dispersion to suspend rock cuttings for subsequent transport – as well as a low plastic viscosity – which minimizes the energy required to pump the fluid downhole at high shear rates.⁸ A proper understanding of the rheology of these clay dispersions and how it evolves with time and the local temperature of the downhole environment is therefore critical for safe and effective drilling operations.

One inorganic clay commonly used in these dispersions is bentonite; a naturally abundant clay comprised of microscopic charged platelets of approximate lateral size ~300 nm. When dispersed in water or brine at appropriate concentrations, the charged bentonite platelets rapidly disperse and produce a viscoelastic yield stress fluid that exhibits a high degree of shear thinning in steady shearing flows, thus simultaneously achieving two essential properties for a drilling fluid.^{2–5} However, accurate rheological characterization of bentonite dispersions is complicated by the fact that the yield stress and viscosity (along with other mechanical properties of the fluid) are not constant in time. Rather, they evolve continuously with time as the small and highly mobile clay platelets self

^a Department of Mechanical Engineering, Massachusetts Institute of Technology, Cambridge, MA, USA. E-mail: gareth@mit.edu

^b Department of Chemical Engineering, Massachusetts Institute of Technology, Cambridge, MA, USA

^c Aramco Services Company: Aramco Research Center, Houston, TX, USA

† Electronic supplementary information (ESI) available. See DOI: <https://doi.org/10.1039/d3sm00492a>

‡ These authors contributed equally to this work.

§ Deceased.



associate in the suspending matrix fluid, a phenomenon known as rheological aging.¹⁰ The additional complexity of incorporating the age of the dispersions as a parameter on which mechanical properties can depend substantially broadens the space of rheological behavior that must be studied, and renders many conventional rheometric tests ineffective.

As an example of the practical effects of this complication, consider the startup of drilling operations after a shutdown. Shutdowns may occur for a number of reasons, including regular maintenance or unforeseen accidents, and their duration is variable. An important requirement for drilling fluids is to rapidly and reversibly develop a yield stress or 'gel strength' to suspend drill cuttings and prevent sedimentation. However, during a shutdown period the rheological properties of a drilling mud or fracturing fluid will continue to evolve with time. For non-aging complex fluids, the operational conditions required to 'break' the gel and restart steady flow in the drill string do not depend on the duration of the shutdown (assuming the shutdown is longer than the longest relaxation time of the fluid). However, for an aging material, key process conditions, such as the applied pressure required to restart flow in the drill strings, do vary with the shutdown duration, possibly dramatically. Anticipating this change is critical to avoid undesirable affects associated with large required pressures for recirculation.¹¹

In this work, we investigate in detail the age-dependent rheological behavior of bentonite dispersions, with the goals of understanding the microstructural origins of aging in these fluids, quantitatively describing this aging process using an appropriate constitutive equation, and examining the effects of aging on the linear and nonlinear rheological properties of the dispersions. We begin with a physical description of bentonite clay and bentonite dispersions in Section 2, which outlines the physical origins of their yield stress and rheological aging, and then describe techniques used to study these features in Section 3. In Section 4, we investigate the age-dependent steady, transient, and dynamic rheological properties of bentonite dispersions using multiple conventional and modern rheometric techniques. Finally, in Section 5 we develop a constitutive model for the age-dependent linear viscoelastic properties of bentonite dispersions, which quantitatively captures the non-ergodic parametric dependence of the linear relaxation modulus and the frequency-dependent complex modulus with both age-time and temperature. Understanding how these aging materials evolve with elapsed time and with temperature renders the model useful for predicting the mechanical response of bentonite-based drilling fluids in many industrially relevant conditions. Moreover, the model for the linear rheology connects the macroscopic physical properties of bentonite dispersions to their microscopic structure, thereby providing experimental evidence for the physical origins of aging in these attractive colloidal dispersions.

Before embarking on a study of the time-dependent mechanical properties of bentonite clay dispersions, it is instructive to clarify the particular terminology used to describe this 'time dependence'. Many terms are employed in the rheology literature to describe the dependence of mechanical

properties with time. One common term, which is often used to describe the evolution of the plastic viscosity and yield stress of drilling fluids,¹³ is 'thixotropy'. The precise definition of thixotropy can vary; some authors adopt a definition which classifies fluids that exhibit a continuous decrease in viscosity during flow (and a subsequent continuous increase in viscosity after cessation of flow) as thixotropic,¹⁴ focusing exclusively on the evolution of inelastic properties with time during or after flow, a response sometimes distinguished as 'ideal thixotropy'.¹⁵ Some adopt a much broader definition by also considering time-evolving changes in viscoelastic properties (such as the relaxation modulus or the storage modulus) that are not associated with the viscoelastic relaxation timescale.¹⁶ Adopting the latter definition, we may view rheological aging as a subset of the broad spectrum of thixotropic effects, in which the evolution of material properties after cessation of flow is perpetual.

Moreover, the phenomenon of rheological aging is often measured through measurements of material properties other than the viscosity (e.g. the complex modulus $G^*(\omega)$), and is driven by evolution in the entire relaxation spectrum (and is therefore not purely inelastic).¹⁵ Rheological aging can also be observed during periods of quiescence, rather than only during or after flow.¹⁷ These are all features of the time-evolution of the mechanical properties of bentonite dispersions, as will become evident through this study. Thus, we adopt the more precise nomenclature of 'rheological aging' for this work.

Although the terms 'thixotropy' and 'rheological aging' are often employed in studies of drilling fluids in the scientific literature, other descriptive terms are perhaps more commonplace in industrial settings. Simple on-site measurements of drilling fluids involve measuring the shear viscosity and 'gel strength' at specified times after the cessation of a short and strong shear flow (e.g. 10 seconds, 10 minutes, and 30 minutes after flow cessation).¹⁸ If the gel strength, which is an approximate measure of the static yield stress, is observed to increase substantially between measurements at subsequent times, the gel is referred to as a 'progressive gel'.¹⁸ Rheological aging gives rise to this type of behavior, as the yield stress and the elastic modulus both increase continuously with time. Progressive gels are often not ideal for drilling applications, as they may require large pumping pressures to restart flow along the drill string, which can lead to undesirable effects such as unwanted hydraulic fracturing. Conversely, a gel whose strength does not increase substantially between two measurements is called 'mild' or 'flat'.¹⁸ Flat gels may still exhibit time-dependent properties on shorter time-scales; however, this time-dependence either arrests entirely or slows substantially, leading to more predictable, and typically lower, required pressures for recirculation.

2 Physical origins of rheological aging in bentonite

Rheological aging is one of the distinct features of clay suspensions, and can be understood directly from physical considerations



of the nano-crystalline structure of bentonite platelets. Sodium bentonite is a montmorillonite clay (see Fig. S1 for the XRD analysis of the sample ESI[†]), composed of discotic crystals with the chemical formula: $\text{Na}_{0.33} [(\text{Al}_{1.67}\text{Mg}_{0.33})(\text{O}(\text{OH}))_2(\text{SiO}_2)_4]$.¹⁹ These discotic crystals are three-layered, composed of tetrahedral structures with silicon and aluminum ions in the center, and octahedral structures with aluminum and magnesium ions in the center. The corners of both the tetrahedral and octahedral structures are either oxygen atoms or hydroxyl groups,^{12,20} with the octahedral structure packed between two tetrahedral layers as shown in Fig. 1(d). Due to the net negative charge of the three-layer crystalline structure, the top and bottom faces of the disc-like crystals carry a negatively charged double-layer, and are therefore associated with free Na^+ cations in solution. The exposed edges of the crystals, on the other hand, reveal the internal metal cations, and therefore generate a positively charged double-layer.²¹

Individual crystals are separated by exchangeable cations and a hydration layer with a typical separation of 10–20 Å.¹⁹ When not dispersed in water, bentonite clay particles are typically 6–200 µm in size⁷ (please see Fig. S2 for the particle size distribution of the anhydrous bentonite particles, ESI[†]). A representative photograph of dry Wyoming bentonite clay is shown in Fig. 1(a), and a scanning electron microscope (SEM) image of these clay particles is shown in Fig. 1(b). When dispersed in water (Fig. 1(c)), these clay particles hydrate and exfoliate into disc-shaped platelets. The major axis of the

individual platelets is approximately 300–500 nm in length, while the minor axis of the platelets is typically in the range of 200–300 nm. These platelets are very thin with thicknesses typically on the order of 1 nm.²²

The process of rheological aging and the development of a viscoelastic gel structure that results in the appearance of a macroscopic yield stress can be rationalized by the different ways in which these platelets associate, and how these associations evolve with time.²³ For bentonite platelets, there are three types of possible associations between two platelets: face-to-face association (FF), edge-to-face association (EF), and edge-to-edge association (EE).²¹ These different platelet configurations are depicted schematically in Fig. 1(e). The relative prevalence of these different modes of association depends on the pH and salt concentration of the aqueous dispersion. For solutions at high pH and high salt concentrations, the double layers on the surface and edges of the crystals are screened; thus the FF mode of interaction dominates. For low pH solutions, when the edges possess a positive charge, the EE and EF associations are more prevalent.^{19,24–27} The coagulation of a bentonite dispersion can be influenced by the addition of inorganic salts. At a neutral pH, the coagulation process is primarily governed by face-face configurations.²⁸ The structural configurations and clusters of bentonite platelets can be influenced and manipulated by the surface chemistry of the material as well. For example, the adsorption of pyrophosphate anions to the edges and polyetheramines to the faces of montmorillonite platelets

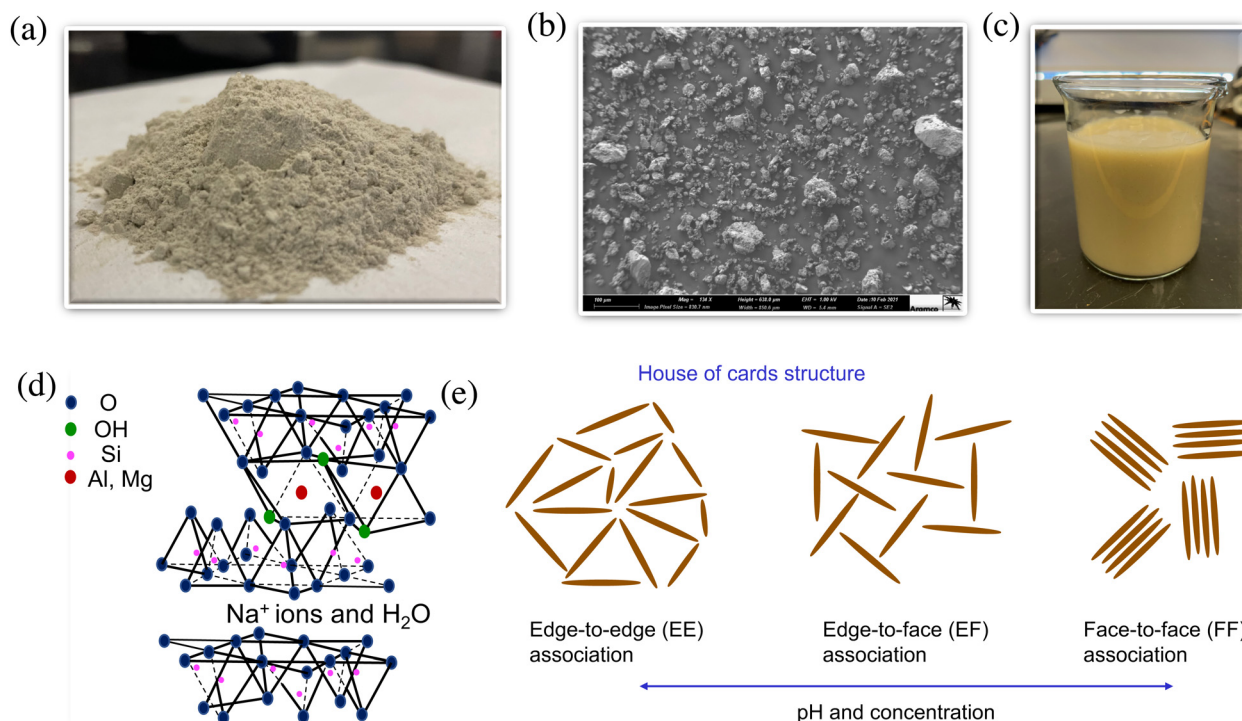


Fig. 1 (a) Photograph of anhydrous Wyoming bentonite clay powder (as received). (b) SEM image of anhydrous bentonite particles. (c) Aqueous dispersion of 5 wt% bentonite. (d) The crystalline structure of Na^+ -montmorillonite platelets, depicting the three-layer structure consisting of outer tetrahedral layers and an inner octahedral layer. Image reproduced from ref. 12. (e) The different modes of association for a dispersion of bentonite platelets.



has been shown to have a controlling effect on these configurations and thus also influences the rheological properties.²⁹

The inter-particle arrangements and relative prevalence of each mode of association influence the strength of the elasto-plastic gel network, including the elastic modulus measured at small strains and the apparent yield stress at large deformations. The average particle anisotropy in a bentonite dispersion can significantly influence the sol-to-gel transition. The concentration required to form a gel increases as the average particle anisotropy increases.³⁰

In a fully *dispersed state* – when the platelets do not form any large-scale structure, and are instead randomly oriented and distributed throughout the medium (*e.g.* as a result of large applied shearing deformations in the recent past) – the elastic modulus of the material is the lowest because of the absence of a sample-spanning microstructure able to distribute an applied load. *Aggregation* due to FF association can similarly decrease the gel strength or elastic modulus by decreasing the number of effective particles in solution.³¹ *Flocculation*, on the other hand, arises from progressive increases in EF or EE association,¹⁹ and is responsible for the appearance and continuous evolution of a gel-like structure. This microstructure is often called a ‘house of cards’ structure.³²

The small size of the disc-shaped Brownian particles that constitute this ‘house of cards’ structure in bentonite dispersions mean they are in continuous motion due to thermal fluctuations, causing a slow but steady structural evolution to form progressively more stable microstructures through the development of ever more EF and EE associations. This self-association underpins the process of rheological aging, and these out-of-thermodynamic-equilibrium materials (which show a progressive slowing of their relaxation dynamics with elapsed time) are often known as *soft glassy materials*.^{33–35} In the process of rheological aging, the characteristic elastic modulus and relaxation time of these materials both increase progressively with time (*i.e.*, the elastic, solid-like character of a soft glassy material increases with time).^{19,34,36–41} Thus, in this soft glassy state, the linear storage modulus is generally significantly greater than the loss modulus (*i.e.*, $G'(\omega, t) \gg G''(\omega, t)$, usually by one order of magnitude), with the storage modulus typically exhibiting a weak power-law dependence on frequency and logarithmic variation in elapsed time.⁴² Finally, we note that by subjecting these materials to large deformations, one can *rejuvenate*, or ‘shear melt’, soft glassy materials by breaking up the developed microstructure, thereby reversing some of the effects of rheological aging.⁴³

3 Materials and methods

The rheological behavior of bentonite is fascinating but at the same time challenging to characterize, because the dispersions exhibit the complex non-ergodic dynamics of rheological aging on top of the rich phenomenology of a viscoelastic yield stress fluid. They may thus be succinctly referred to as thixotropic elasto-viscoplastic (or TEVP) materials.⁴⁴ In Section 4, we

undertake a detailed rheological characterization of these two distinct aspects of the complex thermomechanical response of bentonite. Section 4.1 focuses predominantly on the mechanics of yielding in bentonite dispersions in static, transient, and dynamic contexts. This investigation includes steady shear flow tests, creep tests, and large-amplitude oscillatory shear tests, all of which are commonly employed to characterize soft glassy materials.

In Section 4.2, we study in greater detail the dynamics of aging in bentonite dispersions. In particular, we investigate through stress relaxation experiments and mechanical spectroscopy how the linear viscoelastic response of a bentonite suspension evolves as the material ages. Although the rapid and repetitive nature of step stress relaxation experiments generalize well to aging materials, conventional spectral characterization methods such as small-amplitude oscillatory frequency sweeps do not, because of the sample’s continuous mutation or change in physical properties during the time required to complete a single frequency sweep. Therefore, the present study makes use of a more rapid characterization approach by imposing trains of optimally windowed chirps to distinguish frequency-dependent and age-dependent effects. The data obtained in this latter approach will inform the rheological modeling presented in Section 5 and enable us to systematically unravel how the viscoelastic properties of these aging soft glasses evolve with both time and temperature. Similar stress relaxation tests and conventional frequency sweep experiments have previously been conducted on discotic clays at longer wait times.^{38,40,41} Here, we focus on the less studied challenge of extracting data at short wait times whilst still obtaining valuable mechanistic insights into material thixotropy through incorporation of a novel constitutive framework for modeling rheological measurements of aging materials that are not time-translation invariant.

3.1 Material preparation

The 5 wt% aqueous bentonite dispersion was prepared using dry Wyoming bentonite. First, the bentonite powder was added to water and mixed at 10 000 rpm for 30 minutes using a high shear mixer (Ultra-Turrax T 50 basic mixer, IKA). The dispersion was then placed in a rolling mill for one day to ensure homogeneity and enable the entrained air to separate from the dispersion.

3.2 Rheometry

Rheometric measurements were performed using a controlled stress rheometer (DHR-3 Discovery Hybrid Rheometer, TA Instruments), with a bottom Peltier plate used to set the system temperature, and an upper 60 mm, 2° aluminum cone textured to prevent slip by attaching self adhesive abrasive sandpaper (Trizact A10, 3 M). The cone-and-plate fixture was encapsulated within a solvent trap sealed with water to mitigate solvent evaporation from the sample. Before every experiment, an aliquot of the bentonite suspension was presheared at 500 s^{-1} for 30 s to standardize the initial state and reset the material clock. The ‘wait time’ t_w (or age time) is considered to be the



elapsed time between the cessation of the preshear and the start of an experiment, and the experimental time t is taken to be the total time elapsed after the end of preshear. The test protocols and data acquisition were performed using the rheometer software (TRIOS v5.0.0). In the case of steady shear flow experiments, results from the DHR were also compared to results obtained in an industry-standard FANN 35 A rotational viscometer.

4 Experimental results

4.1 Yielding in bentonite dispersions

4.1.1 Yield stress evolution in steady shear flow. Steady shear flow experiments for bentonite dispersions at different temperatures provide important rheological data that is accessible not just in the laboratory, but on-site in industrial settings. These experiments are used widely in the oil and gas industry to characterize the viscosity of drilling fluids, which undergo different shear histories and experience a wide range of temperatures during the drilling process. In industrial settings, the FANN 35 A rotational viscometer is commonly used to obtain the steady shear flow curve.⁴⁵ To compare our measurements to those available on-site in drilling applications, we collect steady flow curve data using both the more advanced DHR-3 and the industrial FANN viscometer.

In the FANN 35 A viscometer, fluid is contained in the gap between concentric cylinders. The outer cylinder is rotated at a controlled angular speed f (measured in rotations-per-minute, or rpm), and the ensuing motion of the fluid generates a torque on the inner spring-loaded cylinder due to viscous drag, resulting in a small deflection. One degree of deflection corresponds to 0.511 Pa and conversion between rpm in the FANN 35A and the steady shear rate within the fluid is: $\dot{\gamma} = 1.71f$.⁴⁵ There are six speed settings available in the FANN 35 A viscometer: 3, 6, 100, 200, 300, and 600 rpm.

Fig. 2 depicts the measured steady shear stress and the corresponding steady shear viscosity $\eta = \sigma/\dot{\gamma}$ for a 5 wt% bentonite dispersion at room temperature (25 °C), measured with the FANN viscometer (blue circles) and with the DHR at shear rates $\dot{\gamma} \in [1,1000] \text{ s}^{-1}$ with five points per decade (red circles). The stress and viscosity values measured for the six different shear rates from the FANN are in good agreement with the flow curve measured by the DHR for the 5 wt% bentonite dispersion. The shear thinning property of the bentonite dispersion observed in Fig. 2 is one feature that makes this formulation highly desirable for drilling applications, as the bentonite mud can effectively suspend drill cuttings due to its high viscosity at low shear rates while reducing the required pumping power due to its low viscosity at high shear rates.^{46–48}

Having validated the accuracy of the FANN viscometer against the flow curve measured by the DHR rheometer, we next characterized the flow curve of the bentonite dispersion at four different temperatures: 10 °C, 25 °C, 49 °C, and 65 °C, using the controlled stress rheometer. To better resolve the yield stress plateau, we studied a lower range of shear rates,

$\dot{\gamma} \in [0.1,100] \text{ s}^{-1}$, with five points per decade. At each temperature, the shear rate is first progressively increased from 0.1 s⁻¹ to 100 s⁻¹, beginning after a wait time of $t_w = 180$ s, and then progressively decreased from 100 s⁻¹ to 0.1 s⁻¹, beginning at $t_w = 2100$ s. In each direction, the duration of the entire flow sweep was 1800 s. Measurements of the resulting steady shear stress are shown in Fig. 2.

The flow curves depicted in Fig. 2 illustrate two notable features of the steady flow behavior of bentonite. Firstly, rheological hysteresis is evident in the upwards and downwards sweeps in Fig. 2(b), as the steady shear stress measured during the decreasing shear rate sweep is higher than that measured by the earlier increasing shear rate sweep, particularly at low shear rates. For clarity, only room temperature (25 °C) data is shown in the plot; however, flow curves at other test temperatures display similar qualitative features, and are presented in the ESI.[†] The observed hysteresis is due to the gradual build-up of the gel-like microstructure^{49,50} as the shear rate is progressively decreased, leading to a stronger gel developing in the decreasing-rate sweeps especially at low rates, (corresponding to longer sample age times) whereas the same development of structure of the bentonite platelets cannot occur in the shorter elapsed time between the initial preshear and the first low-rate measurements in the increasing-rate sweeps. Ultimately, the flow curves for the increasing- and decreasing-rate sweeps converge at high shear rates above 50 s⁻¹, as the gel-like structure is broken down faster than it can be rebuilt, and viscous dissipation dominates the observed rate-dependent response.

The second important characteristic of these flow curves is that they exhibit the expected shape for a yield-stress fluid with shear-thinning characteristics. Flow curves of this form are well-described by the simple viscoplastic Herschel–Bulkley model:

$$\sigma(\dot{\gamma}) = \sigma_y + k\dot{\gamma}^n \quad (1)$$

where σ_y is the (dynamic) yield stress and k and n are the consistency and shear thinning parameters respectively. The data presented in Fig. 2(c), corresponding to the increasing-rate sweep data only (for clarity), are fit to the Herschel–Bulkley model using nonlinear least-squares regression, providing quantitative estimates for the yield stress σ_y in the increasing-rate sweeps as a function of temperature. It is also important to note that soft glassy materials, like bentonite dispersions, may potentially exhibit transient or steady-state shear banding at low shear rates due to rheological aging or inherent non-monotonic flow curves.^{23,51–54} These phenomena may not be apparent from traditional bulk rheometry techniques, consequently when reporting the precise values of the yield stress for practical applications, caution must be exercised due to the possibility of shear banding. Corresponding fits were also performed for the decreasing-rate sweeps (and are shown in the ESI,[†] for clarity). From these fits we observe that the yield stress in both the increasing- and decreasing-rate sweeps is larger at higher temperatures as shown in Fig. 2(d). These experiments are conducted at $T \in [10, 25, 37, 49] \text{ }^\circ\text{C}$ (50–140 F) since the typical surface temperature can vary from 10 °C to



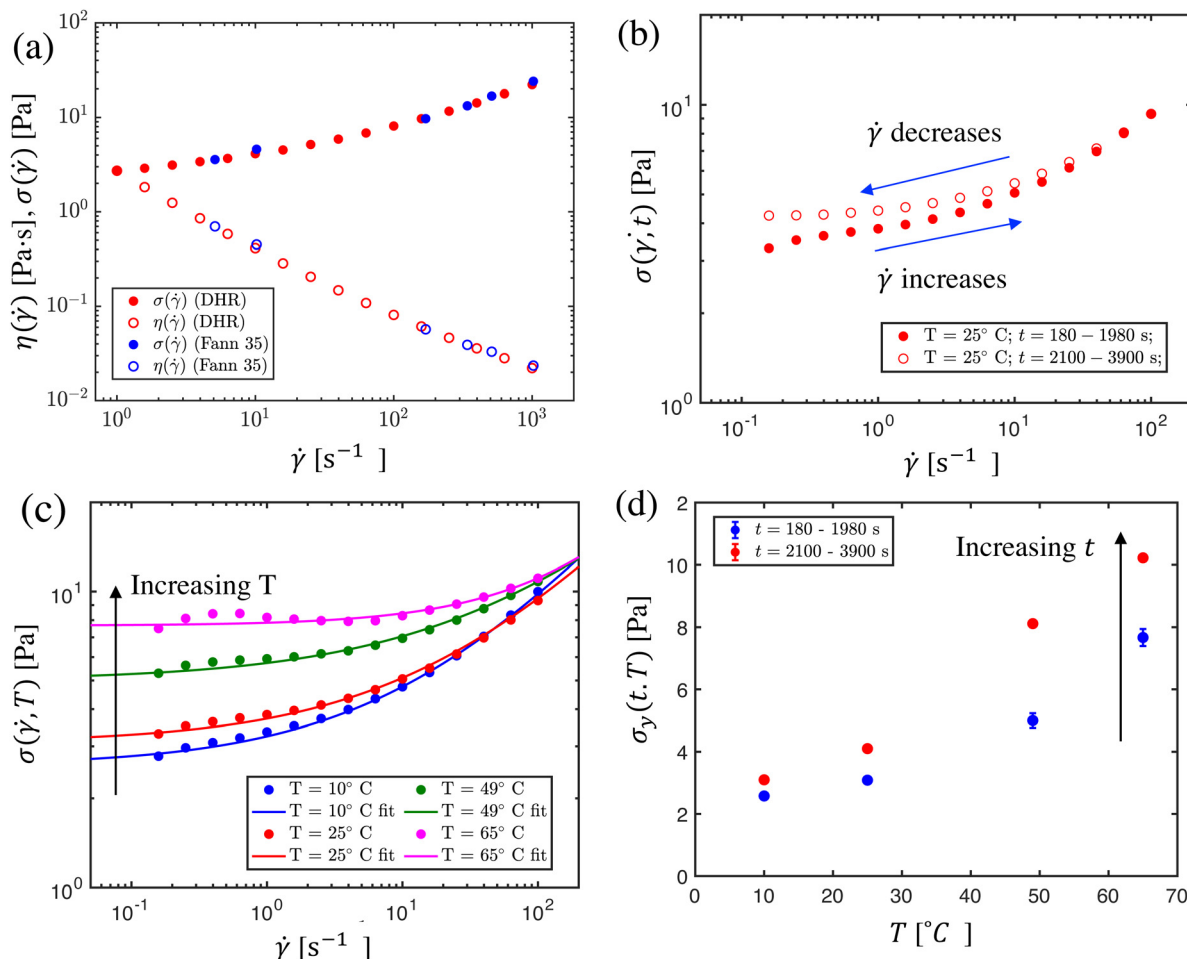


Fig. 2 The steady flow curve for bentonite dispersions at different temperatures and age times. (a) Comparison of the steady shear stress (filled circles) and viscosity (unfilled circles) measured by the FANN 35A viscometer (blue) and DHR-3 rheometer (red) for a 5 wt% aqueous bentonite dispersion at room temperature (25 °C). (b) The flow curve measured at room temperature by an increasing-rate sweep and decreasing-rate sweep, showing hysteresis due to rheological aging. (c) Flow curves measured at different temperatures via increasing-rate sweeps. The Herschel Bulkley (HB) model, $\sigma = \sigma_y + k\dot{\gamma}^n$, is fit to the data to calculate the apparent dynamic yield stress. The parameters of the HB fits for different temperatures $T = 10$ °C, 25 °C, 49 °C and 65 °C are: $\sigma_y = 2.5$ Pa, 3 Pa, 5 Pa, and 7.6 Pa; $k = 0.66$ Pa sⁿ, 0.64 Pa sⁿ, 0.73 Pa sⁿ and 0.17 Pa sⁿ; and $n = 0.52$, 0.49, 0.44 and 0.64, respectively. (d) The apparent dynamic yield stress at each measured temperature for increasing- and decreasing-rate sweeps. Please see Fig. S3 (ESI†) for the decreasing-rate sweeps and their corresponding Herschel Bulkley fits.

40 °C, depending on the geographical location.²⁷ This observed temperature dependence of yield stress is in agreement with other studies of bentonite dispersions,^{7,22,55} and is thought to result from increases in thermal motion accelerating the formation of EF and EE associations, driving the glassy microstructure deeper into a state of low free energy and leading to a more stable gel structure.

4.1.2 Transient yielding during creep. Steady flow sweeps characterize the dynamic yielding and shear thinning behavior of bentonite suspensions in a manner that is simple enough to be reproduced on-site, while still providing sufficient data to compare and discriminate between the expected rheomechanical response of bentonite dispersions at different temperatures. These measurements even provide a glimpse into the evolution of the yielding and flow properties of bentonite dispersions that result from rheological aging. However, yielding is a fundamentally transient phenomenon, a feature not

fully captured by steady flow experiments. Moreover, the transient signatures of sample yielding are intertwined with the dynamics of rheological aging. Creep tests are an effective method for measuring and understanding this aspect of yielding and flow in bentonite dispersions.

We first conducted creep tests for a range of applied stresses $\sigma_0 \in [0.1, 10]$ Pa at $T = 25$ °C, and for a wait time of $t_w = 60$ s after preshear. The evolution of the accumulated strain, as shown in Fig. 3(a), depends sensitively on the applied stress. It has been proposed that these strain trajectories can be classified into three distinct regimes, based on the applied stress.¹⁰ In the *solid-like* regime, the applied stress is less than a value called the *first critical stress*, σ_{c1} . In this regime, the applied stress does not generate enough shear to break down the gel microstructure faster than it is rebuilt due to thermal motion. This results in a progressive decrease in the rate of shearing, and eventual cessation of flow. Another regime is characterized by applied

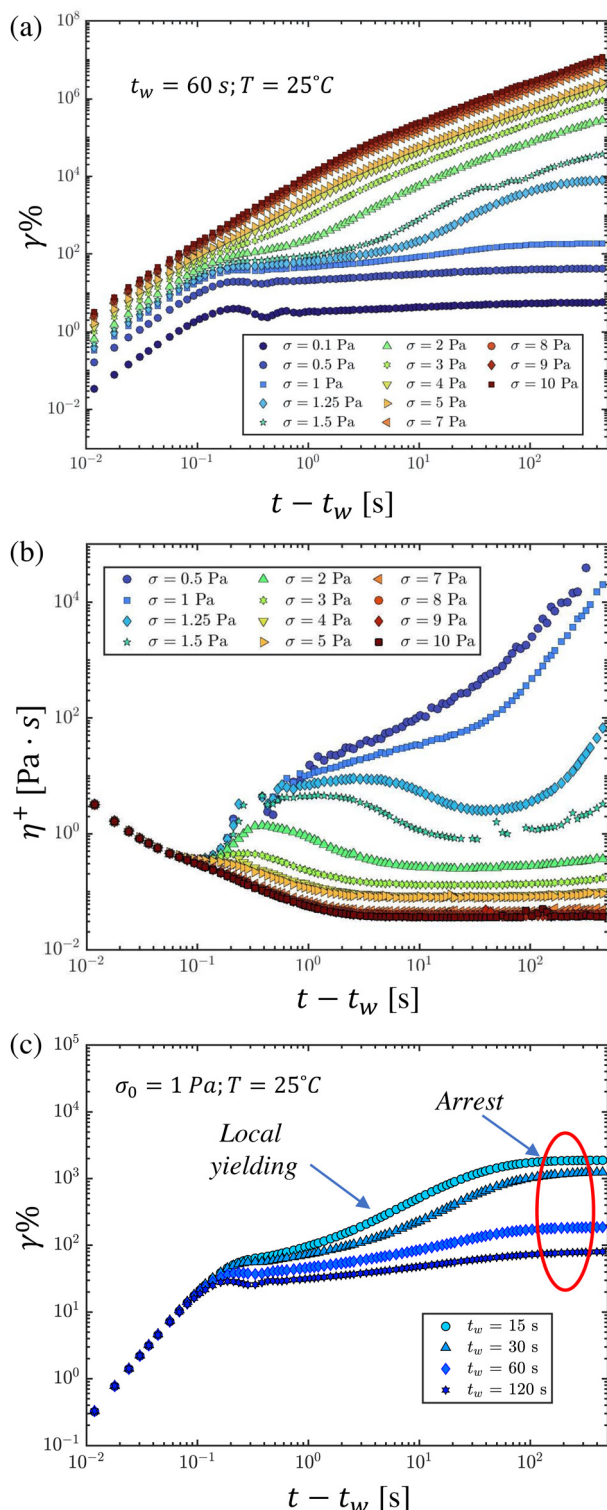


Fig. 3 (a) Creep experiments in a 5% bentonite clay for various applied stresses are shown, with a fixed wait time of $t_w = 60$ s. The critical stress, $\sigma_{c_1} = 1$ Pa and the second critical stress, $\sigma_{c_2} = 2$ Pa, may be determined by transitions in the shapes of the creep transients. (b) The plot of apparent viscosity η_{app} obtained from creep experiments, showing the viscosity bifurcation occurring at approximately $\sigma_{c_2} = 2$ Pa. (c) Creep experiments with an applied stress of $\sigma = 1$ Pa conducted for various wait times, t_w , which show a dependence of the material response on the age of the dispersion when the applied stress is under σ_{c_2} .

stresses greater than the *second critical stress*, σ_{c_2} . In this regime, the applied stress imposes sufficient shear strain in the sample to break down the microstructure faster than it can be rebuilt, leading to a net breakdown of structure and increase in the rate of shearing to an eventual steady rate, which is set either by the balance between structural breakdown and build up, or by viscous dissipation in the dispersion at very high rates. Fluids in this regime may be described as exhibiting *viscoplastic liquid-like* behavior, and the second critical stress is typically considered to be the static yield stress of the material.¹⁰ More complex effects such as transient shear banding may also develop in the material.²³

In the intermediate regime between σ_{c_1} and σ_{c_2} , more complicated *elastoviscoplastic* (EVP) transients are observed, representing the complex interplay between structural breakdown due to both the accumulated strain, the stress-activated rate of microstructural breakdown and the structural build-up with time. Initially, the young sample is at its most disordered, and therefore continues to build up internal structure. This build-up eclipses the initial rate of breakdown, causing a decrease in the instantaneous rate of shearing. However, as the rate of aging slows in the soft glassy material, the shear has not decreased to complete cessation, and eventually structural breakdown overtakes microstructure formation, resulting in a delayed yielding and transition to a steady flow. This slow flow is not steady in time, however, and fluctuations in the local microstructure eventually may lead to cessation of flow.¹⁰

This complex phenomenon is generically known as *viscosity bifurcation*,⁵⁶ and can be seen in the evolution of the apparent viscosity $\eta_{app}(t, \sigma_0) = \sigma_0/\dot{\gamma}(t_{age})$ evolution with time of creep as illustrated in Fig. 3(b), where flow curves measured at high applied stress stabilize at low values of the steady-shear viscosity, while a bifurcation is observed at a critical stress corresponding to σ_{c_2} , after which (*i.e.*, $\sigma < \sigma_{c_2}$) the curves tend towards infinite viscosities at long times.

These three classes of yielding transients, and the corresponding viscosity bifurcation, are evident in both Fig. 3(a), which depicts the accumulated strain after loading, and Fig. 3(b), which depicts the evolution in the apparent viscosity defined as $\eta_{app}(t, \sigma_0) = \sigma_0/\dot{\gamma}(t)$. In all cases there is an initial inertial response of the instrument (corresponding to the quadratic increase in strain at early times⁵⁷). For the 5 wt% bentonite dispersion there is a monotonic decrease in the rate of shearing $\dot{\gamma}(t)$ – or equivalently a monotonic increase in the apparent viscosity for applied stresses below $\sigma_{c_1} = 1$ Pa. A more complex intermediate, transient elastoviscoplastic creep response is observed for curves between this first critical stress and the second critical stress of approximately $\sigma_{c_2} = 2$ Pa. Beyond σ_{c_2} , the transient motion always evolves to a steady shearing deformation (with the shear strain increasing as $\gamma \sim \dot{\gamma}t$) and the viscoplastic material ‘flows’.

It is clear from these results and accompanying discussion that the transient creep dynamics of bentonite below the second critical stress, σ_{c_2} , are sensitive to the rate of physical aging, which itself depends on the rheological age of the dispersion and also on the wait time t_w since the initial

preshear. We investigate this sensitivity by holding the applied stress constant at $\sigma_0 = 1$ Pa, and instead varying the wait time t_w before the load is applied. The resulting creep trajectories are depicted in Fig. 3(c). For small wait times, we observe an elastoviscoplastic response characteristic of the intermediate regime, $\sigma_{c_1} \leq \sigma_0 \leq \sigma_{c_2}$. However beyond a waiting time of $t_w = 60$ s the material has sufficiently aged that it responds (at this level of applied stress) as a viscoelastic solid.

4.1.3 Dynamic yielding in oscillatory loading. The previous steady flow and creep experiments studied the yielding characteristics of bentonite dispersions during steady shear-rate and stress loading. However, the rich phenomenology of yielding extends to dynamic loading conditions as well. Large amplitude oscillatory stress (LAOS) tests are an effective means for probing the dynamic yielding behavior of yield stress fluids such as bentonite.^{58–60} In a LAOS test, a shear stress waveform, $\sigma(t) = \sigma_0 \sin(\omega(t - t_w))$ is applied beginning at the end of the wait time t_w , and the output strain or strain rate measured. One convenient tool for visualising LAOS data is the Lissajous curve, which parameterically represents the shear stress $\sigma(t)$ on one axis and the shear strain $\gamma(t)$ (or strain rate $\dot{\gamma}(t)$) on the other. The shape of these Lissajous curves indicate important features about the material response at the time scale dictated by ω and the deformation scale dictated by σ_0 , such as whether the experiment is in the linear or nonlinear deformation regime, and whether energy storage (elastic effects) or energy dissipation (viscous effects) is dominant.

In Fig. 4, we depict Lissajous curves taken at $T = 25$ °C for four frequencies $\omega \in [0.3, 10]$ rad s⁻¹ and six stress amplitudes $\sigma_0 \in [0.1, 6]$, with a wait time of $t_w = 300$ s. Before we interpret these curves in the context of dynamic yielding, we note that it is important in stress-controlled dynamical tests such as LAOS to assess sources of instrumental bias – in this case, inertia from the cone-and-plate fixture at high frequencies and high amplitudes. To quantify such effects, we apply the dimensionless ‘inertia number’ In , defined by Dimitrou *et al.* as the ratio of inertial torque T_i and sample torque T_s .⁶⁰ For a cone-and-plate fixture with radius R and angle θ_0 , the inertial torque $T_i \approx I\omega^2\theta_0\gamma_0$ and the sample torque is given by $T_s \approx \frac{2\pi\sigma_0R^3}{3}$, thus the inertia number is:

$$In = \frac{3I\omega^2\theta_0\gamma_0}{2\pi\sigma_0R^3} \quad (2)$$

where I is the total moment of inertia of the fixture (and rheometer) and γ_0 is the amplitude of the strain response. For LAOS measurements to avoid significant inertial bias, the inertia number should be small, with $In < 0.05$ taken as a typical criterion. In Fig. 4, experiments that exceed this limit are shown on a dark shaded background. In order to extract meaningful information about the material response from these curves, inertial corrections must be applied by subtracting the inertial torque T_i due from the measured total torque.⁶⁰

With inertial corrections in place, the Lissajous curves may be used to extract information about dynamic yielding in bentonite dispersions. One useful heuristic for characterizing

the extent of dynamic yielding from these curves is the normalized area fraction,⁶⁰ defined as:

$$\phi = \frac{E_d}{(E_d)_{pp}}, \quad (3)$$

where E_d is the energy dissipated in one cycle and $(E_d)_{pp}$ is the energy dissipated by a hypothetical ‘perfectly plastic’ material with a load of equal amplitude. These energies are related to the area of the corresponding Lissajous curves:

$$E_d = \sigma d\gamma, \quad (4)$$

$$(E_d)_{pp} = (\sigma_{\max} - \sigma_{\min})(\gamma_{\max} - \gamma_{\min}). \quad (5)$$

This area fraction ϕ takes on particular values for perfectly plastic, Newtonian, and purely elastic materials:

$$\phi = \begin{cases} 1 & \rightarrow \text{Plastic} \\ \pi/4 = 0.785 & \rightarrow \text{Newtonian} \\ 0 & \rightarrow \text{Elastic} \end{cases} \quad (6)$$

This area fraction ϕ is also reported for every Lissajous curve in Fig. 4. For low stress amplitudes, the Lissajous curves are elliptic, meaning the material response is approximately linear viscoelastic in character. Moreover, ϕ is nearly zero for these low-amplitude measurements across the frequency range, indicating a predominantly elastic, solid-like response. With increasing stress amplitude, the Lissajous curves widen, indicating a more dissipative viscoelastic response. At intermediate stress amplitudes the material response is clearly nonlinear and fully elastoviscoplastic models^{60–62} are required to describe the stress-dependent and frequency-dependent yielding dynamics. At the highest stress amplitude of $\sigma_0 = 6$ Pa, ϕ exceeds the value for a Newtonian fluid. For these largest stress amplitude experiments, therefore, the dispersion appears to dynamically yield and flow. For these high amplitude, viscoplastic-like responses, we observe that ϕ decreases with increasing frequency, indicating that the extent to which the dispersion yields has decreased. Thus, dynamical yielding in bentonite dispersions appears to be frequency-dependent, with an apparent yield stress that increases with increasing frequency, or decreasing deformation time-scale.

From the flow curve experiments at various temperatures discussed in Section 4.1.1, it is observed that the yield stress *increases* with temperature. Therefore, we expect the plastic flow regimes observed in LAOS tests to occur at higher imposed stress amplitudes as the temperature increases. However, it is important to note that despite these changes, we can still anticipate qualitatively similar Lissajous curves characterized by a transition from a predominantly linear elastic response at small strains to a non-linear viscoelastic response, and eventually to a plastic (yielding) response, as the imposed oscillatory stress increases. The principal difference would be that each of these material state transitions will occur at higher stress amplitudes with increasing temperature.



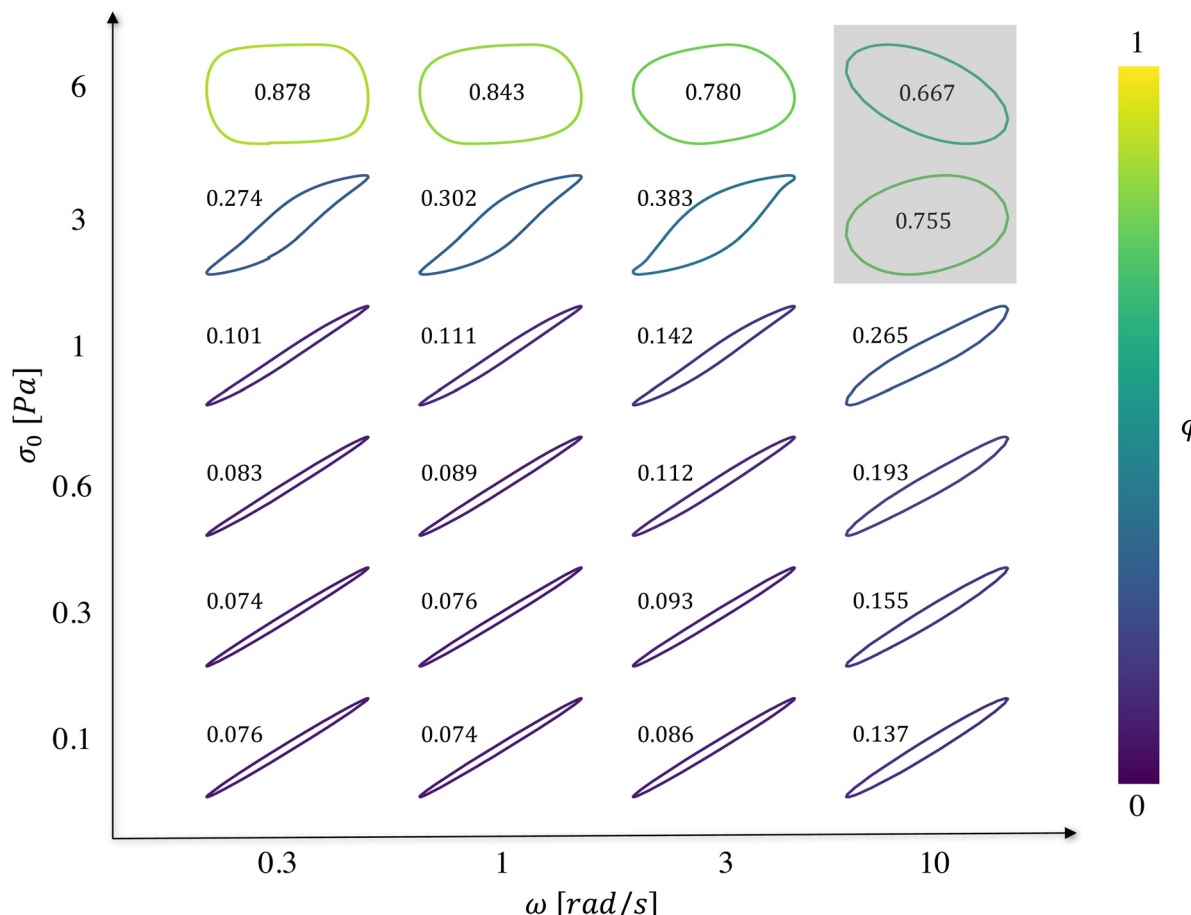


Fig. 4 Lissajous curves for large amplitude oscillatory shear (LAOS) experiments for a 5 wt% bentonite dispersion at $T = 25$ °C and an age time of $t_w = 300$ s over a set of stress amplitudes σ_0 and angular frequencies ω . The area criterion for yielding ϕ is shown for each LAOS experiment, demonstrating a transition towards dynamic yielding (larger ϕ) with increasing stress amplitudes. At the highest stress amplitude, the normalized area ratio decreases with angular frequency, suggesting a lower extent of yielding and a time-scale (or frequency) dependent dynamic yield stress. The Lissajous curves for input stress of amplitudes $\sigma_0 = 3$ and 6 Pa, with an angular frequency $\omega = 10$ rad s⁻¹ (shown on a gray background), are dominated by inertial effects ($\ln > 0.05$) and hence do not provide meaningful information.

4.2 Rheological aging in bentonite dispersions

The previous sections detailed three nonlinear rheological tests, which revealed a rich phenomenology of wait-time, temperature, and deformation time-scale-dependent yielding in bentonite dispersions. In some instances, we investigated the dependence of these effects on rheological aging; however, the high-dimensional state and response spaces of nonlinear rheological tests make a detailed quantification and constitutive modeling of rheological aging in this soft glassy material difficult. To simplify this modeling challenge, we turn instead to linear rheological studies. In linear time invariant (LTI), non-aging systems, the linear stress relaxation modulus depends only on the elapsed time since the imposition of the deformation, $G(t - t_w)$. One common description of rheological aging for non-LTI systems is that the linear relaxation modulus is parametric in the wait time since initial sample preparation or resetting of the material clock by preshear, $G(t - t_w, t_w)$.¹⁷ Similarly, treating t_w parametrically and assuming the material response is pseudo-steady in t_w , we may define a linear complex modulus, $G^*(\omega, t_w)$.

A natural way to characterize the wait time-dependent relaxation modulus is through stress relaxation tests, performed at different wait times. This is sufficient for a non-LTI system, because in defining $G(t - t_w, t_w)$ we have only assumed that the step strain is applied instantaneously at t_w . However, in defining the complex modulus $G^*(\omega, t_w)$, we have assumed that the material response is pseudo-steady in t_w , meaning that the material does not substantially age during the time required to perform an experimental measurement at frequency ω . For traditional small amplitude frequency sweeps, which take minutes to complete, this criterion is clearly not satisfied. Therefore, we must turn to modern techniques with higher time resolution to characterize $G^*(\omega, t_w)$ within the pseudo-steady approximation. Here, we employ exponential chirps, which take only ~ 10 seconds to characterize $G^*(\omega, t_w)$ over one order of magnitude in frequency. As with the stress relaxation experiments, we may apply these chirps at successive wait times, to characterize the linear viscoelasticity of the suspensions as a function of both time-scale and material age.

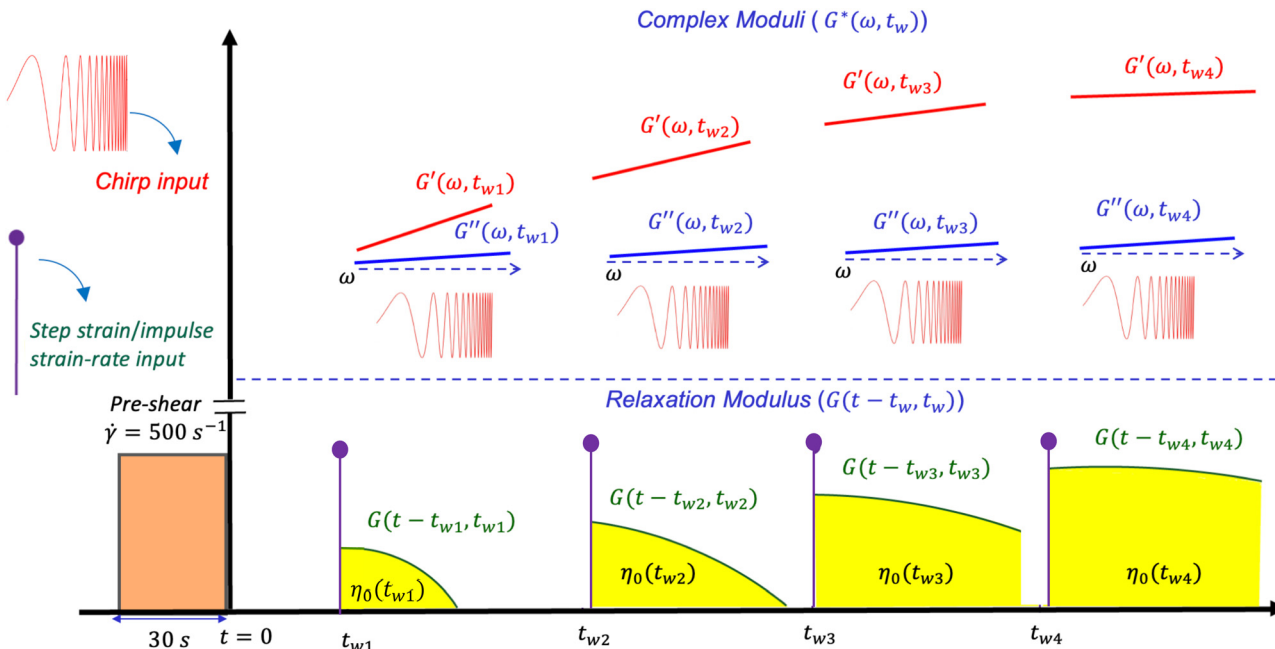


Fig. 5 Schematic representation of the experiments used to characterize the linear viscoelasticity of bentonite dispersions as a function of both the deformation-time scale and the age of the material. After preshear, step strain experiments and chirp experiments are conducted sequentially at different wait times to obtain the relaxation modulus and complex modulus, respectively. Due to aging, the modulus increases and the relaxation dynamics slow down with wait time. These phenomena can be observed in both the relaxation modulus and frequency response. The zero-shear viscosity may be computed from the area under the stress relaxation curves, which also demonstrates an increase in the viscous response with age.

A schematic diagram of the data collected by applying optimally windowed, exponential chirps, along with stress relaxation experiments, to bentonite dispersion is presented in Fig. 5.

4.2.1 Stress relaxation after step strain. We conduct stress relaxation experiments at four temperatures, $T = 10\text{ }^\circ\text{C}$, $25\text{ }^\circ\text{C}$, $37\text{ }^\circ\text{C}$, and $49\text{ }^\circ\text{C}$, by applying a strain of $\gamma_0 = 2\%$ at various wait times $t_w \in [45, 400]\text{ s}$. The resulting shear stress $\sigma(t - t_w, t_w)$ is measured and used to compute the stress relaxation modulus: $G(t - t_w, t_w) = \sigma(t - t_w, t_w)/\gamma_0$. The strain amplitude γ_0 was selected to ensure linearity by imposing multiple step strains with varying γ_0 , and choosing a value that was sufficiently in the range of amplitudes for which the measured $G(t - t_w, t_w)$ was independent of the amplitude. The data obtained at $T = 10\text{ }^\circ\text{C}$ are depicted in Fig. 6. Data at the remaining temperatures share many of the same qualitative features as the data in this figure, and are presented in the Fig. S4 (ESI†).

The stress relaxation experiments at fixed temperature reveal two important features of rheological aging, both of which are in agreement with our physical description of aging in bentonite dispersions in Section 2 and with the previous experimental results. Firstly, the relaxation modulus increases with t_w at each temperature. This increase is simply a result of the stronger, more developed microstructure in dispersions that have undergone more aging, compared to the relatively weak character of the young dispersions. Secondly, the relaxation modulus decays faster for small wait times, corresponding to a progressive slowing of relaxation dynamics with rheological

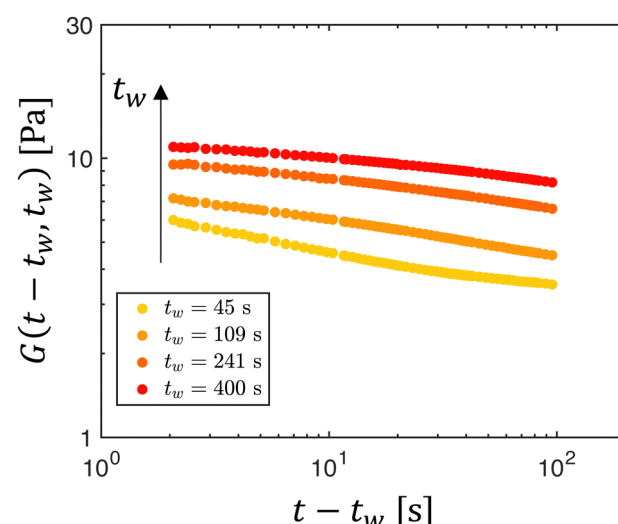


Fig. 6 (a) The relaxation modulus for different wait times at $T = 10\text{ }^\circ\text{C}$, showing an increase in the modulus and increase in the relaxation time with the age of the dispersion. The step strain amplitude imposed for all the experiments at different temperatures is $\gamma_0 = 0.02$.

aging as the system gradually settles into a more energetically stable microstructural state. In some of the shortest wait time experiments (e.g., the wait time of 45 s in Fig. 6), we also observe a long-time plateau in the relaxation modulus *i.e.*, the system mechanically ‘arrests’. This is another notable feature of rheological aging systems, but its origins from physical



considerations are less obvious. In the Appendix, we instead explore the origins of this feature from a modeling perspective, which incorporates phenomenological theories of rheological aging. Moreover, in Fig. 5, we note that the area under the stress relaxation curves is equivalent to the zero-shear viscosity $\eta_0(t_w)$; thus, the data in Fig. 6 indicate graphically that the system's viscosity increases as the suspension ages.

4.2.2 Optimally windowed chirps. When performing rheological characterization of the viscoelastic properties of non-aging materials, it is common to conduct sweeps across a range of frequencies to measure the dynamic response of a material across vastly different time-scales. These frequency sweeps, however, may require observations over the course of many minutes, and therefore are not well-posed for materials that age on a shorter timescale. Instead, we turn to an experimental protocol that provides similar information to the conventional frequency sweep, but in a much shorter window of observation: exponential chirps. Here, we apply a sequence of optimally windowed exponential chirps,^{63–65} with input stress signals of the form:

$$\sigma(t) = \sigma_0 \begin{cases} \cos^2\left[\frac{\pi}{r}\left(\frac{t}{T} - \frac{r}{2}\right)\right] \sin\left[\frac{\omega_1 T}{\log(\omega_2/\omega_1)}\left[\exp\left(\log(\omega_2/\omega_1)\frac{t}{T}\right) - 1\right]\right] & \frac{t}{T} \leq \frac{r}{2} \\ \sin\left[\frac{\omega_1 T}{\log(\omega_2/\omega_1)}\left[\exp\left(\log(\omega_2/\omega_1)\frac{t}{T}\right) - 1\right]\right] & \frac{r}{2} < \frac{t}{T} < 1 - \frac{r}{2} \\ \cos^2\left[\frac{\pi}{r}\left(\frac{t}{T} - 1 + \frac{r}{2}\right)\right] \sin\left[\frac{\omega_1 T}{\log(\omega_2/\omega_1)}\left[\exp\left(\log(\omega_2/\omega_1)\frac{t}{T}\right) - 1\right]\right] & \frac{t}{T} \geq 1 - \frac{r}{2} \end{cases} \quad (7)$$

In our experiments the period of the chirp is $T = 14$ s, the cutoff frequencies are $\omega_1 = 0.3$ rad s⁻¹ and $\omega_2 = 5$ rad s⁻¹. Since we are working with a shorter chirp signal (time-bandwidth TB = $T(\omega_2 - \omega_1)/(2\pi) = 10.62 < 100$), windowing the exponential chirp signal is essential to reduce spectral leakage and restore general periodicity in the output signal. This enables a reduction in oscillatory errors in the moduli measurements.⁶⁴ In the present study, we utilize a Tukey window with a tapering parameter of $r = 0.1$ combined with our exponential chirp, as it has been shown to be the optimal window for obtaining rheological measurements.⁶⁴ The imposed stress amplitude is $\sigma_0 = 0.1$ Pa and is far below the yield stress of the dispersion even at short age times. Because we have confirmed using stress relaxation experiments that stress signals of this amplitude do not alter the microstructure of bentonite, we may interpret each successive chirp as an independent measurement of the frequency spectrum of the aging dispersion, as though the material had remained undisturbed until the time t_w at which the chirp signal begins. We treat each chirp as an “instantaneous” measurement, which is of course a coarse approximation at early times. However, it is important to note that as the wait time increases in an aging material the mutation number monotonically decreases. This decrease occurs due to the progressive slowing down in the rate of aging with time, resulting in progressively improved accuracy in the localization and computation of the complex moduli as the wait time increases and the chirp duration becomes much smaller than the sample age.⁵⁰

The storage and loss moduli measured by a series of ten chirps at $T = 10$ °C are presented in Fig. 7. The storage modulus measured by each chirp increases with the age time of the dispersion and displays a weak power-law dependence with frequency, consistent with previous observations and theoretical predictions for soft glassy materials.^{17,33} The loss modulus, on the other hand, remains relatively insensitive to both the imposed frequency and to the age of the suspension. Although these qualitative observations are consistent with the physical description of rheological aging in bentonite suspensions, obtaining deeper quantitative insight into the data requires the development of an appropriate viscoelastic constitutive model, which is the focus of the next section.

5 Modeling linear viscoelasticity and rheological aging in bentonite suspensions

We now seek to develop a constitutive model, based on the data obtained from the chirp experiments and stress relaxation

experiments reported in the previous section, to enable prediction of the linear rheological properties of aging bentonite dispersions over a range of time scales and temperatures. To describe the time-, age-, and temperature-dependent linear

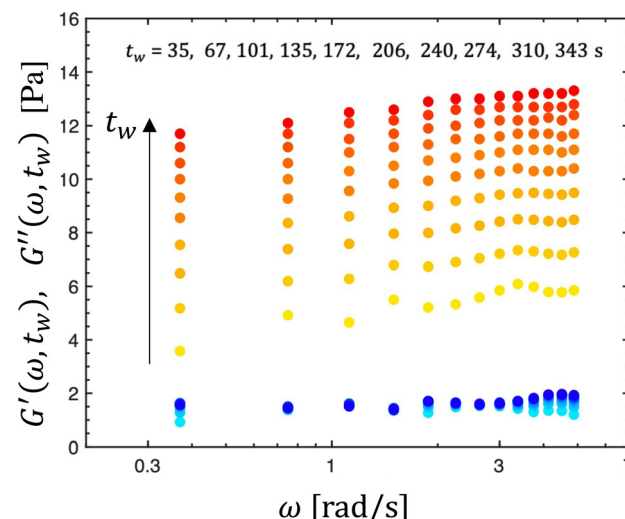


Fig. 7 The evolution of the storage and loss moduli with wait time t_w as measured by a sequence of optimally windowed chirps, at $T = 10$ °C. The storage modulus (> 3 Pa for all wait times) transitions from yellow to red filled circles with increasing wait time. The loss modulus (< 3 Pa for all wait times) transitions from light to dark blue with increasing wait time.



viscoelastic behavior of the bentonite dispersions, we will proceed in three steps. First, we supply the hypothesis that the microstructure within the dispersion responds to imposed deformations or loading on a time scale proportional to its characteristic relaxation time, while this relaxation time itself increases as the material ages. Thus, we may rescale the 'laboratory' (or real) time coordinate by this relaxation time to obtain an effective 'material time', in which the microstructural response appears constant. This process of 'time-age-time superposition' (TATS) generates a master curve of the relaxation and complex modulus in the material time and frequency domain for each temperature. With this transformation complete, the next step in modeling is to select a constitutive equation to describe the linear viscoelastic response in material time. Here, we employ the Fractional Maxwell Gel (FMG) model for this purpose. Finally, we may use the parameters of the FMG model fits at each temperature to shift the individual TATS master curves obtained at each temperature onto a single superposed 'grand master curve', representing 'time-age-time-temperature superposition' (TATTS) of the data. The resulting constitutive model accounts both for the temperature-dependent dynamics and aging of the linear response. It can then be used to predict the TATS master curves over a range of temperatures, and remapping the time coordinate of each master curves to the laboratory time produces predictions for the evolution in the relaxation modulus $G(t - t_w, t_w, T)$ and complex modulus $G^*(\omega, t_w, T)$ at any intermediate time or temperature.

5.1 Transformation to material time

As a result of aging, the Boltzmann superposition principle does not hold for the linear rheology of the bentonite dispersion.^{34,66} For systems in which the relaxation modulus is age-time dependent, the stress must be written in the form:¹⁷

$$\sigma(t) = \int_{-\infty}^t G(t - t', t') \dot{\gamma}(t') dt'. \quad (8)$$

Joshi and coworkers have shown this aging effect can often be understood as a change in the material's relaxation time scale as the material ages. A common model for describing the evolution of the material relaxation time is one in which the relaxation time scales with the age time of the material raised to a power-law exponent μ .^{33,34,36-38,67,68} We may therefore define a 'material time' ξ , which casts the elapsed laboratory time between t and t_w in an aging reference frame, relative to the aging material relaxation time:⁶⁶

$$\xi(t) - \xi(t_w) = \int_{t_w}^t \left(\frac{t_R}{t'}\right)^\mu dt', \quad (9)$$

where t_w is the wait time defined previously and t_R is an arbitrarily selected reference time. When $\mu = 0$, the material does not age, and the regimes where $\mu > 1$ and $\mu < 1$ are called hyperaging and subaging, respectively.⁴² A discussion of common signatures of hyperaging for soft glassy materials is presented in the Appendix. The limiting case where $\mu = 1$ is referred to as simple aging.¹⁷

Now, considering the elapsed time in the material time domain, the output stress can be written in terms of the Boltzmann superposition integral with the effective relaxation modulus \tilde{G} defined in the material time domain:^{34,36,42}

$$\sigma(\xi) = \int_{-\infty}^{\xi(t)} \tilde{G}(\xi - \xi') \frac{dy}{d\xi} d\xi', \quad (10)$$

where the elapsed time in the material time domain is related to the laboratory time by integrating eqn (9):

$$\frac{\tilde{t}}{t_R} = \frac{\xi(t) - \xi(t_w)}{t_R} = \frac{1}{1-\mu} \left[\left(\frac{t}{t_R}\right)^{1-\mu} - \left(\frac{t_w}{t_R}\right)^{1-\mu} \right]. \quad (11)$$

Following Shukla *et al.*,³⁸ the relaxation modulus in the laboratory time frame $G(t - t_w, t_w)$ may be converted to the effective relaxation modulus \tilde{G} in the material time domain by multiplying with a vertical shift factor $b(t_w)$, which accounts for the age-dependent modulus scale:

$$\tilde{G}(\tilde{t}) = b(t_w)G(\tilde{t}, t_w) \quad (12)$$

The vertical shift factor $b(t_w)$ shifts the transformed curves to a single master curve on the material time $\tilde{t} = \xi(t) - \xi(t_w)$ axis. To obtain the effective complex modulus \tilde{G}^* in the effective frequency domain $\tilde{\omega}$, we apply a Fourier transform with respect to the material domain variables \tilde{t} and $\tilde{\omega}$

$$\tilde{G}^*(\tilde{\omega}) = i\tilde{\omega} \int_0^\infty \tilde{G}(\tilde{t}) e^{i\tilde{\omega}\tilde{t}} d\tilde{t}. \quad (13)$$

Although eqn (12) is sufficient to describe experimental data, there may be instantaneous, non-aging background effects (e.g. from the solvent, or other non-aging viscous dynamics) not evident in stress relaxation data measured at finite times. These effects do influence the complex modulus at all frequencies, however, and must be accounted for first to obtain good data superposition. A similar non-aging contribution to the total stress was observed in Shukla *et al.*³⁸ for aging LAPO-NITE® dispersions at high frequencies and at long age times ($t_w > 1000$ s), which they described in terms of a viscoelastic response with a short characteristic relaxation time. With these effects of non-aging accounted for, we obtain:

$$\tilde{G}^*(\tilde{\omega}) = b(t_w)[G^*(\omega(t_w/t_R)^\mu, t_w) - i\eta_0\omega], \quad (14)$$

where η_0 represents a background viscosity that accounts for the non-aging, Newtonian effects that occur in parallel with the aging relaxation mode. Here we may also write the effective frequency $\tilde{\omega}$ in the material domain in terms of the actual imposed laboratory frequency ω :

$$\tilde{\omega} = \omega \left(\frac{t_w}{t_R}\right)^\mu. \quad (15)$$

These equations represent a general framework for time-age-time superposition (TATS). However, a quantitative description of the linear viscoelastic properties of bentonite at a fixed temperature still requires a mechanical model for the relaxation modulus $\tilde{G}(\tilde{t})$ and complex modulus $\tilde{G}^*(\tilde{\omega})$ in the material time domain.



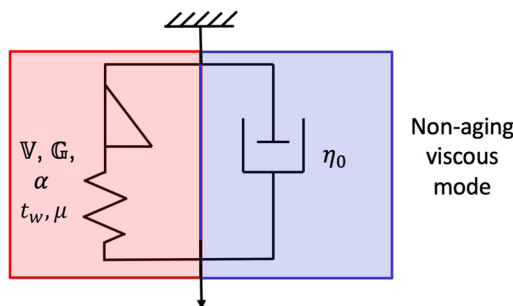


Fig. 8 Proposed mechanical model for the aging linear viscoelastic response of the 5 wt% bentonite dispersion, which is composed of an aging FMG model in parallel with a non-aging viscous mode.

5.2 The fractional Maxwell gel model in material time

One phenomenological viscoelastic model that is capable of describing many of the qualitative features of the linear rheology of bentonite is the fractional Maxwell gel (FMG) model.^{69,70} In what follows, we model the linear rheology of bentonite by applying the FMG model to describe the component of the rheological response that ages, and adding a non-aging viscous element in parallel to describe background solvent effects. The proposed micromechanical model is shown in Fig. 8.

The constitutive equation for the aging FMG^{69,70} in the material time domain is:

$$\tilde{\sigma}(\tilde{t}) + \frac{V}{G} \frac{d^{\alpha} \tilde{\sigma}(\tilde{t})}{d\tilde{t}^{\alpha}} = V \frac{d^{\alpha} \tilde{\sigma}}{d\tilde{t}^{\alpha}}, \quad (16)$$

where $\tilde{\sigma}$ is the stress in the material time domain and V, G and α are the parameters of the FMG model. Dimensional considerations show that G is a modulus with SI units of [Pa] and V is a quasistatic property with units [Pa s $^{\alpha}$].⁶⁹ The contribution to the total stress for the non-aging viscous mode, σ_v , in laboratory time is given by:

$$\sigma_v(t) = \eta_0 \dot{\gamma}(t). \quad (17)$$

Combining these stresses in parallel, in the real or laboratory time domain, the total stress can be written using eqn (9), (10) and (12) as follows:

$$\sigma(t - t_w, t_w) = \tilde{\sigma}(\tilde{t})/b(t_w) + \sigma_v(t - t_w), \quad (18)$$

with \tilde{t} given by eqn (11).

In order to fit the viscoelastic response of the bentonite dispersion in the material time domain using the FMG model, the non-aging viscous mode should first be subtracted from the total real-time response. The relaxation modulus for the model sketched in Fig. 8 in the real time domain is given by the expression:

$$G(t - t_w, t_w) = \frac{1}{b(t_w)} G E_{\alpha,1} \left(-\frac{G}{V} \tilde{t}^{\alpha} \right) + \eta_0 \delta(t - t_w), \quad (19)$$

where $E_{\alpha,1}(z)$ is the two-parameter Mittag Leffler function.^{63,69,71} Similarly, the frequency-dependent complex modulus in the

laboratory time domain is:

$$G^*(\omega, t_w) = \frac{1}{b(t_w)} \frac{V(i\tilde{\omega})^{\alpha}}{1 + \frac{V}{G}(i\tilde{\omega})^{\alpha}} + i\eta_0 \omega. \quad (20)$$

In total, this linear viscoelastic model for the bentonite dispersion is a five parameter model, with one undetermined function $b(t_w)$ of the wait time. The three parameters V, G, α parameterize the aging FMG model with the characteristic material time scale:

$$\tilde{\tau} = \left(\frac{V}{G} \right)^{(1/\alpha)}. \quad (21)$$

The aging exponent μ describes the dilation of time in conversions between laboratory time and material time (see eqn (11)), and the parameter η_0 accounts for the viscosity of the non-aging viscous solvent mode.

5.3 Fitting the model to experimental data

To fit the exponentially-measured chirp and stress relaxation data at a fixed temperature to the proposed constitutive model, we first determine the values of η_0 , μ , and the set of $\{b(t_w^{(i)})\}$ for each $t_w^{(i)}$ within the data set, which optimally superpose the data onto separate master curves for the relaxation modulus and complex modulus (using eqn (11), (12) and (14) with a reference time of $t_R = 400$ s). This fitting is done by visual inspection. For the $T = 10$ °C data, the optimal values for η_0 and μ were found to be $\eta_0 = 0.15$ Pa s and $\mu = 1.6$, which were validated using a automated technique for data superposition we have recently developed.⁷² For determining the vertical shift factors ($\{b(t_w^{(i)})\}$) from measurements of the evolving complex moduli in the post-gelled bentonite dispersion, it is convenient to use the age-dependent storage modulus data ($G'(\omega, t_w)$) data because it is not influenced by the non-aging solvent contribution to the oscillatory stress (which affects measurements of the viscous loss modulus). However, at early times, when the dispersion is in a pre-gel case, and the dominant contribution to the stress is the aging viscous response, more robust determination of the vertical shift factors can be obtained from the loss moduli data ($G''(\omega, t_w)$).⁷³ Once these master curves were constructed, they were fit to the FMG model (eqn (19) and (20)) simultaneously using nonlinear least-squares regression, giving parameter values of $G = 17.8$ Pa, $V = 46.5$ Pa s $^{\alpha}$, $\alpha = 0.24$ and $\tilde{\tau} = 54.7$ s for the $T = 10$ °C data. The resulting master curves and model fit for this temperature, both in the material time and the laboratory time, are shown in Fig. 9.

This time-age-time superposition (TATS) process, and the subsequent regression of the master curve to the FMG model, was repeated for the experimental data at each temperature. The fits to the relaxation modulus in material time and laboratory time for temperatures $T = 25$ °C, $T = 37$ °C, and $T = 49$ °C are shown in the Fig. S5 (ESI†). Master curves for the relaxation modulus at each temperature are presented in Fig. 10(a). In the fits of these master curves to the FMG model, we have constrained $\eta_0 = 0.15$ Pa s and $\alpha = 0.24$ at every temperature. The latter of these assumptions is necessary such



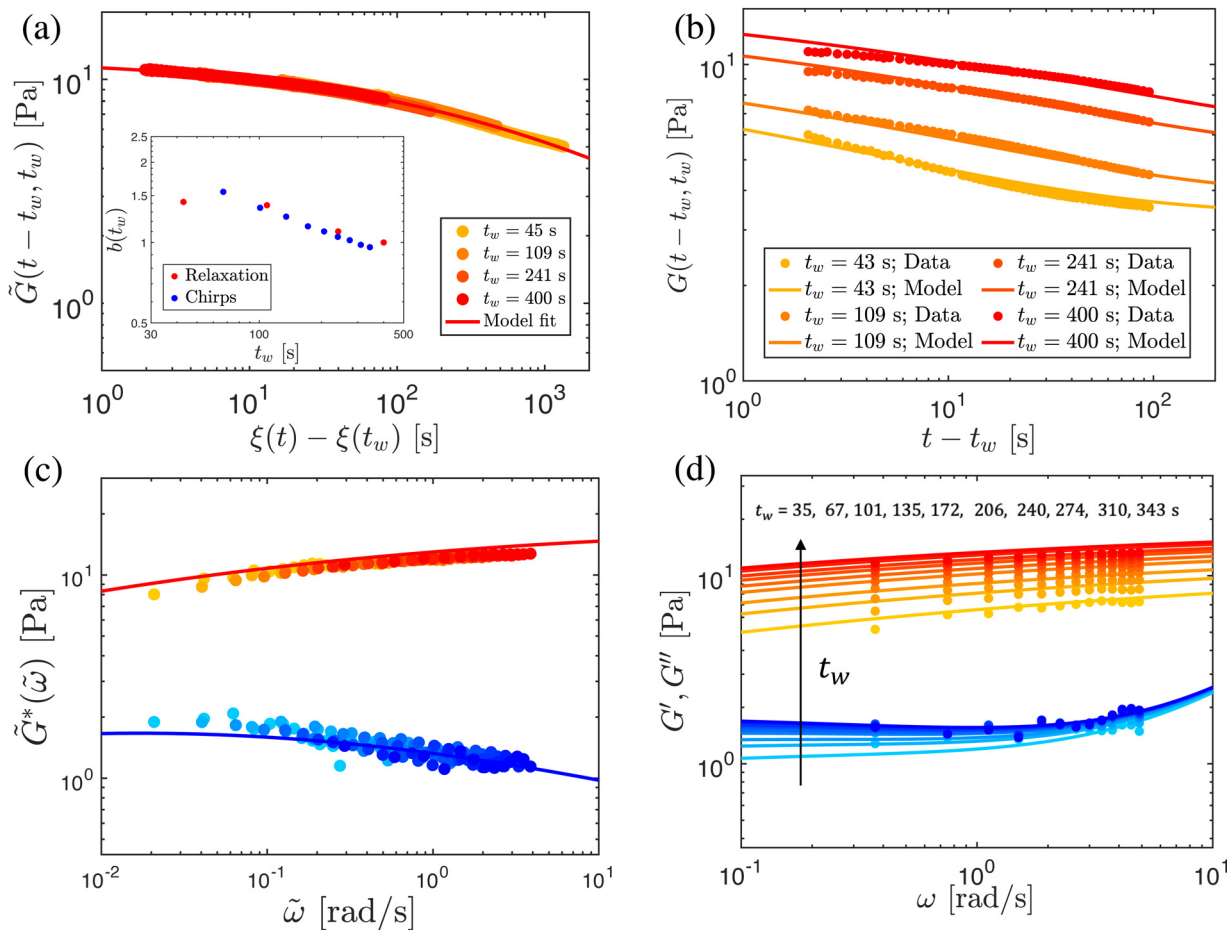


Fig. 9 (a) The relaxation modulus and (c) the complex modulus in the material time and material frequency domains at $T = 10$ °C, respectively, along with (b) the raw relaxation modulus data in laboratory time and (d) the raw chirp data as a function of imposed laboratory frequency. The data points in (a) and (c) are those from (b) and (d) transformed to material time and frequency using the parameters $\mu = 1.62$, reference time of $t_R = 400$ s, and vertical shift factors $b(t_w)$ (shown in inset of (a)), after having subtracted out the viscous mode with constant viscosity $\eta_0 = 0.15$ Pa s. The fits to these time–age time master curves represent the FMG model with $\mathbb{G} = 17.79$ Pa, $\mathbb{V} = 46.52$ Pa s $^\alpha$, and $\alpha = 0.24$. The model fits to the master curves are then transformed to laboratory time and frequency and shown alongside the raw data in (b) and (d). The symbol color changes from yellow to red (for the relaxation and storage moduli) and from light to dark blue (for the loss modulus) with increasing wait time t_w .

that the model itself is parametrically self-similar in temperature. That is, in order to superpose these TATS master curves onto a time–age–time–temperature (TATTS) grand master curve at a reference temperature (T_{ref}), we must have that the FMG model predictions at temperatures T_{ref} and T are related by horizontal and vertical shift factors a_T and b_T , respectively (note that b_T here is a shift factor with respect to temperature, distinct from the $b(t_w)$ shift factors used for TATS):

$$\frac{\mathbb{V}(T_{\text{ref}})(i\tilde{\omega})^\alpha}{1 + \frac{\mathbb{V}(T_{\text{ref}})}{\mathbb{G}(T_{\text{ref}})}(i\tilde{\omega})^\alpha} = b_T \frac{\mathbb{V}(T)(i\tilde{\omega}/a_T)^\alpha}{1 + \frac{\mathbb{V}(T)}{\mathbb{G}(T)}(i\tilde{\omega}/a_T)^\alpha} \quad (22)$$

or

$$\mathbb{G}(T_{\text{ref}})E_{\alpha,1}\left(-\frac{\mathbb{G}(T_{\text{ref}})}{\mathbb{V}(T_{\text{ref}})}\tilde{\tau}^\alpha\right) = b_T \mathbb{G}(T)E_{\alpha,1}\left(-\frac{\mathbb{G}(T)}{\mathbb{V}(T)}(a_T\tilde{\tau})^\alpha\right) \quad (23)$$

where $(\mathbb{V}(T_{\text{ref}}), \mathbb{G}(T_{\text{ref}}))$ and $(\mathbb{V}(T), \mathbb{G}(T))$ are the FMG model parameters determined at the selected reference temperature

(T_{ref}) and an individual test temperatures (T), respectively. For eqn (22) and (23) to hold requires that the horizontal and vertical shift factors a_T and b_T are given by:

$$a_T = \frac{\tilde{\tau}(T)}{\tilde{\tau}(T_{\text{ref}})}, \quad b_T = \frac{\mathbb{G}(T_{\text{ref}})}{\mathbb{G}(T)}, \quad (24)$$

where the characteristic relaxation time constants at each temperature are $\tilde{\tau}(T_{\text{ref}}) = \left(\frac{\mathbb{V}(T_{\text{ref}})}{\mathbb{G}(T_{\text{ref}})}\right)^{1/\alpha}$ and $\tilde{\tau}(T) = \left(\frac{\mathbb{V}(T)}{\mathbb{G}(T)}\right)^{1/\alpha}$.

Thus, by fitting the FMG model to the data sets obtained at each temperature with α held constant, we may construct the grand master curve directly from the regressed model parameters. The constraint that $\alpha = 0.24$ for all temperatures does not affect the quality of the fits, as evidenced by Fig. 10(a), supporting the hypothesis of parametric self-similarity in temperature. The grand master curve of the stress relaxation data constructed via this procedure (with $T_{\text{ref}} = 49$ °C) is shown in



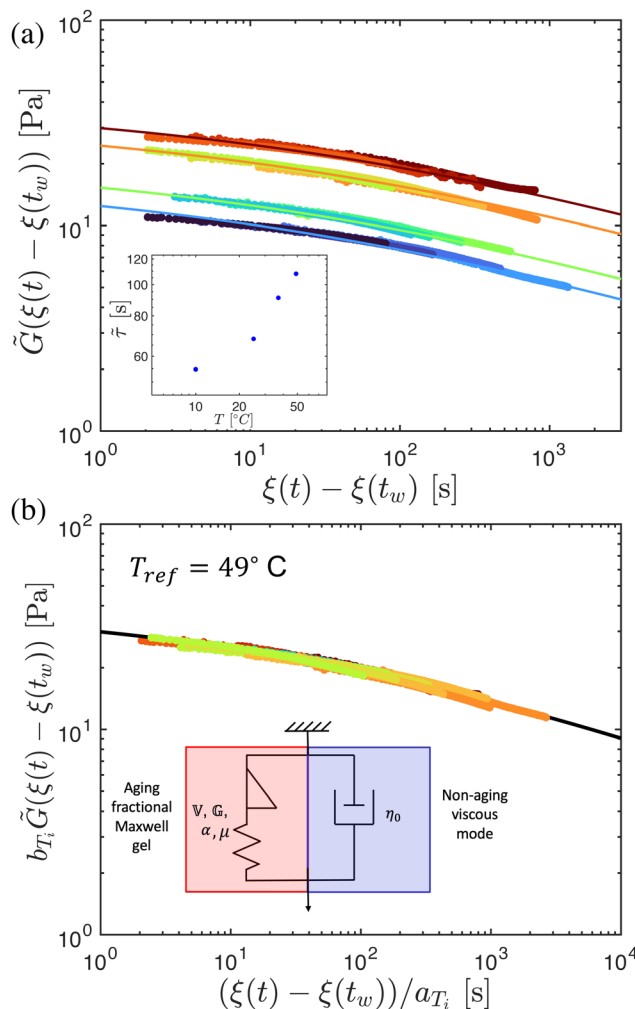


Fig. 10 The development of a time-age-time-temperature superposition grand master curve for the stress relaxation data. (a) The time-age-time master curves obtained at each of the four temperatures studied in this work. (b) All stress relaxation data superposed into a single grand master curve with a reference temperature of $T = 49$ °C. The grand master curve is fit to the FMG model (shown in the inset) with $\mathbb{G} = 40.7$ Pa, $\mathbb{V} = 125.3$ Pa s 2 , and $\alpha = 0.24$. This model fit, along with the shift factors necessary for temperature superposition and the transformations (i.e. the parameters $\mu(T)$, η_0 , and $b(t_w)$) used for wait time superposition, allow for prediction of the relaxation modulus and complex modulus for this bentonite dispersion at any temperature and wait time within the studied range.

Table 1 Values of the fitted model parameters for bentonite dispersion at different temperatures. The reference temperature $T_{ref} = 49$ °C is considered for calculating horizontal shift factors a_T and vertical shift factors b_T

T [°C]	\mathbb{G} [Pa]	\mathbb{V} [Pa s 2]	α	μ	η_0	$\tilde{\tau}$ [s]	a_T	b_T
10	17.8	46.5	0.24	1.62	0.15	54.7	0.50	2.28
25	21.5	59.3	0.24	1.45	0.15	67.9	0.63	1.89
37	33.8	99.8	0.24	1.32	0.15	91.0	0.84	1.20
49	40.7	125	0.24	1.20	0.15	108	1	1

Fig. 10(b), and the values of the model parameters for each temperature are tabulated in Table 1.

One observation of note from the grand master curve is that the horizontal shift factors a_T increase monotonically with temperature, corresponding to an increase in the characteristic relaxation time, while the vertical shift factor b_T decreases with temperature, corresponding to an increase in the modulus scale. This increase in the modulus is likely attributable to the increased rate of microstructural rearrangement due to enhanced thermal motion, which leads to the faster development of a stronger microstructure. We may also attribute the increase in the characteristic relaxation time with temperature to these stronger microstructures, though this effect may be confounded with other effects, such as faster energy dissipation due to enhanced thermal fluctuations, which would tend to decrease the relaxation time.

6 Discussion

Although the aging FMG model is valuable on its own as a predictive tool for describing the rheology of bentonite dispersions at different temperatures, certain aspects of the model may be interpreted in a physical context as well, and may therefore provide a connection between the microscopic structure of bentonite dispersions and their mechanical properties. In particular, it has been previously reported that the aging exponent $\mu(T)$ is a linear function of $1/T$.⁴⁰ We find that this functional form describes our data well, as illustrated in Fig. 11(a). The best fit for μ with $1/T$ is determined by least-squares regression to be:

$$\mu(T) = \frac{980}{T} - 1.8. \quad (25)$$

The inverse-temperature dependence of $\mu(T)$ originates from Arrhenius-type arguments, specifically that:⁶⁷

$$\mu \propto \frac{G_0 l^3}{k_B T}. \quad (26)$$

Here, we see that μ is the ratio of an elastic energy scale $G_0 l^3$ and a thermal energy scale $k_B T$ in the thermally aging soft glass, where k_B is Boltzmann's constant, G_0 is a characteristic elastic modulus, and l is a characteristic length scale of the particles in the dispersion. Assuming that $G_0 \approx 10$ Pa from the order of magnitude of the linear viscoelastic data, and taking $\mu = 1.6$ at $T = 10$ °C we obtain an estimate of l to be 10^{-7} m, which is on the same order of the length scale of the bentonite particles as observed from SEM images (Fig. 1(b)). This suggests that the model presented in this work indeed connects bulk rheological observations to microstructural theories for disc-shaped particles. Our findings on the aging exponent μ , yield stress σ_y and the elastic modulus G' of bentonite dispersions are also consistent with the recent findings of Bhattacharyya and coworkers²³ that thixotropic materials which show a time dependent yield stress also show hyperaging behavior ($\mu > 1$) and a noticeable increase of the elastic modulus $G'(t - t_w, t_w)$ with age time. We also note that the magnitude of the non-aging solvent viscosity η_0 does not affect the aging exponent μ since the latter parameter is relevant only to the age-dependent

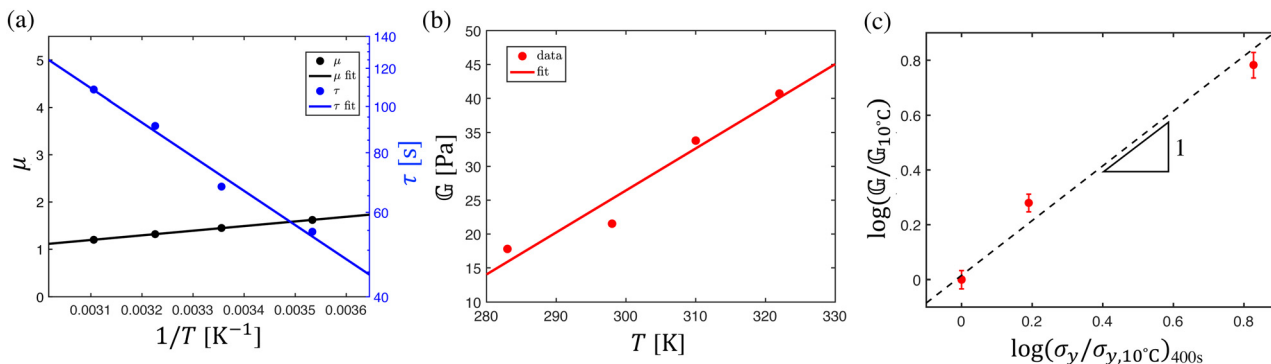


Fig. 11 (a) The characteristic relaxation time computed from the FMG model as a function of temperature (blue circles). The logarithm of this relaxation time varies with the inverse of the temperature (fit shown by a solid line), which may be used to predict the characteristic relaxation time at intermediate temperatures. The aging exponent μ as a function of temperature (black), also shows an approximately linear dependence on the inverse of the temperature (fit shown by a solid line). This allows for μ to be predicted at intermediate temperatures, and the slope of this fit may be correlated to microstructural properties in the dispersion. (b) Evolution of the elastic modulus G as a function of temperature (red circles), fit to a linear function in the temperature (solid line) to allow for interpolation at intermediate values. (c) Comparison of the yield stress and FMG modulus as a function of temperature, accounting for rheological aging. A proportionality line with unit slope is shown by a dashed line, to indicate that the yield stress is approximately proportional to the FMG modulus, and therefore the elastic modulus determined from the FMG aging model may be used to predict the yield stress as a function of both temperature and age.

contribution to the total state of stress in the bentonite dispersion. Based on the available experimental evidence there does not appear to be a direct correlation between the relaxation exponent α (characterizing the frequency dependence of the viscoelastic spectrum at a fixed age time) and the aging exponent μ (characterizing the evolution of the material properties with age time).

In motivating this study of bentonite dispersions, we noted that it is critical to anticipate the physical properties of suspensions in industrial applications, such as drilling operations. In those circumstances, however, nonlinear properties such as the yield stress of the suspension are also important. It is difficult to model these nonlinear properties for an aging dispersion; thus, we have focused in the previous section on modeling the linear thermorheological properties of the suspension. In our discussion of the physical origins of aging in Section 2, we noted that the elastic strength of the suspension in the linear regime and the yield stress both relate to the same physical feature: the continuously aging gel microstructure. Thus, our model for aging in the linear response may provide useful predictions for nonlinear properties as well, such as the yield stress.

To examine the correlation between the linear model and nonlinear properties, we cross plot the yield stress and the linear viscoelastic modulus determined from the FMG model in Fig. 11(c). The measurements of the yield stress corresponds to increasing shear-rate sweeps (flow curve) beginning at $t_w = 180$ s, whereas the FMG modulus corresponds to a reference wait time of $t_w = 400$ s. Thus, we first correct for aging in the yield stress by interpolating the vertical shift factors $b(t_w)$ determined for the stress relaxation data using eqn (19). With this correction in place, we see that a log-log plot of σ_y vs. G reveals a near linear relationship with a slope near unity, corresponding to linear proportionality between G and σ_y . Thus, in practice, our model for the linear response of

bentonite suspensions, which accounts for both temperature- and age-related effects, may be used to predict the gel modulus G at a particular wait time and temperature, and this prediction can subsequently be correlated to the anticipated static yield stress. This procedure may be of direct utility in industrial drilling applications, where the evolution of the yield stress of the drilling fluid after a period of shutdown is a critically important property.

7 Conclusions

As evidenced by the richness of the data sets presented throughout this work, the thermomechanical behavior of bentonite dispersions in shear is quite complex. In steady shear, creep, and LAOS tests, we have observed the rich phenomenology of an aging yield–stress fluid, with a temperature-dependent yield stress plateau, multi-step transient yielding, and an apparent dynamic yielding transition that depends on the deformation time-scale. The yield stress, as well as the transient signatures in the creep compliance observed below this stress, depend on the age of the material as well as its temperature, with older dispersions appearing stronger due to the development of a more stable microstructure. In drilling applications, the temperature- and age-dependence of this yielding transition highlights the importance of understanding the fluid's rheology for safe and efficient operations. During shut-downs the time at which drilling fluids remain at rest, along with the downstream temperature, can be used to anticipate the additional pumping power required to restart flow.

The inherent complexities introduced by plasticity and aging in the nonlinear rheology of bentonite dispersions renders modeling difficult in that regime. However, the signatures of aging are still evident in the linear response, and therefore we have developed a quantitative model to describe the observations from small-amplitude oscillatory chirp and linear stress relaxation data. This model captures the power-law aging in the mechanical



properties of bentonite and the linear viscoelastic response in the reduced ‘material time’ domain is well-described by a fractional Maxwell gel (FMG) model. Moreover, the response is self-similar in temperature, and therefore measurements at different temperatures may be collapsed onto a ‘grand master curve’ to allow for rapid predictions of the evolving linear rheological properties of the aging gel at different temperatures and wait times. Not only does this time–age–time–temperature (TATTS) framework provide a predictive tool for describing the linear viscoelastic properties of the bentonite dispersions, but the aging dynamics observed at different temperatures are consistent with certain microscopic physical properties of the material, such as an intrinsic modulus and the size of platelets. Recognizing these connections, it may be possible to directly apply the same modeling framework outlined in this work to other discotic clay dispersions with varying particle sizes. We have also documented a linear correlation between the elastic strength of the material in the linear regime and the yield stress at the same age time allowing the model we have developed to describe both aging and temperature effects in the linear viscoelastic response of the dispersion to also provide quantitative predictions of the evolution in the sample yield stress, which is relevant to industrial operations with such aging materials.

In developing an appropriate model for the linear viscoelasticity of this bentonite dispersion, we required data that spanned a two-dimensional domain: capturing variations in both the deformation time-scale ($t - t_w$), and the material age (t_w). Many commonplace techniques for characterizing the linear response of soft materials, in particular small-amplitude frequency sweeps combined with Fourier transform analysis, cannot provide adequate resolution in age time (due to the elapsed time required to sweep over a range of frequencies), and this convolves the effects of stress relaxation and rheological aging. Thus, the study of rapidly aging soft materials represents a particularly suitable application of modern rheometric techniques, such as the optimally windowed exponential chirps employed in this work. Rheological aging also highlights the need for particular care in developing and employing rheometric techniques that provide high data-density to enable systematic transformation to the material time domain and construction of time–age–time–temperature (TATTS) master curves. Such experiments are crucial for resolving the additional complexities of rheologically aging viscoelastic materials.

Conflicts of interest

There are no conflicts to declare.

Appendix

Appendix: Signatures of hyperaging ($\mu > 1$)

Hyperaging ($\mu > 1$) soft glassy materials exhibit unique signatures in their linear dynamics, which can be visually identified

in experimental data. Here, we explore characteristic signatures of hyperaging materials in stress relaxation experiments. For $\mu > 1$, it is perhaps more instructive to write eqn (11) as follows:

$$\frac{\tilde{t}}{t_R} = \frac{\xi(t) - \xi(t_w)}{t_R} = \frac{1}{\mu - 1} \left[\left(\frac{t_R}{t_w} \right)^{\mu-1} - \left(\frac{t_R}{t} \right)^{\mu-1} \right], \quad (27)$$

where t_w is the time elapsed between the cessation of preshear and the beginning of an experimental measurement, and t is the total elapsed time since the cessation of preshear. For $t > t_w$, eqn (27) makes clear that the elapsed material time \tilde{t} is nonnegative and increases (nonlinearly) with laboratory time scale t .

The dependence of the material time interval \tilde{t} on the elapsed laboratory time $t - t_w$ since the beginning of an experiment at time $t = t_w$ is illustrated in Fig. 12, which plots eqn (27) for a set of distinct age times t_w . Each of these curves is observed to approach an asymptote as the wall clock time $t \rightarrow \infty$. The asymptotic value can be derived by direct inspection of eqn (27) in that limit:

$$\lim_{t \rightarrow \infty} \frac{\xi(t) - \xi(t_w)}{t_R} = \frac{\tilde{t}_{\text{asym}}}{t_R} = \frac{1}{\mu - 1} \left[\left(\frac{t_R}{t_w} \right)^{\mu-1} \right] \quad (28)$$

The asymptotic value of the material time coordinate depends on the wait time t_w , the aging exponent μ , and also on the value selected for the arbitrary reference time t_R . Moreover, closer inspection of eqn (27) reveals that this asymptote is unique to hyperaging materials; for subaging materials ($\mu < 1$), the material time interval \tilde{t} increases in time without bound.

The presence of an asymptote in the material time interval is a consequence of the superlinear evolution of the sample’s relaxation time with the laboratory time t for $\mu > 1$. The superlinear dependence of the relaxation timescale τ on the age time of the material leads to a divergence in the amount of time needed for a fixed *absolute* magnitude of stress in the material to decay. As a result, the material approaches a structurally arrested state, beyond which it is unable to further relax. The inverse dependence of the asymptotic material time interval \tilde{t} on t_w predicted by eqn (28) is due to the acceleration in aging that occurs between preshear and t_w . The dependence of \tilde{t} on t_R is simply due to the arbitrary scale of the material time coordinate set by the reference time. When the reference time of choice (t_R) is kept the same for all experimental observations it has no bearing on the actual predictions of the model.

Although mathematically the asymptotic value of the material time interval, \tilde{t}_{asym} , is formally reached only at infinite laboratory time, we may make an estimate of the finite laboratory time at which the plateau in the material time is practically reached in experiment. At short laboratory time scale $\frac{t - t_w}{t_w} \ll 1$, the evolving material time \tilde{t} is linearly dependent on the laboratory time (or wall clock) t :

$$\lim_{t \rightarrow 0} \xi(t) - \xi(t_w) = \left(\frac{t_R}{t_w} \right)^\mu (t - t_w) \quad (29)$$



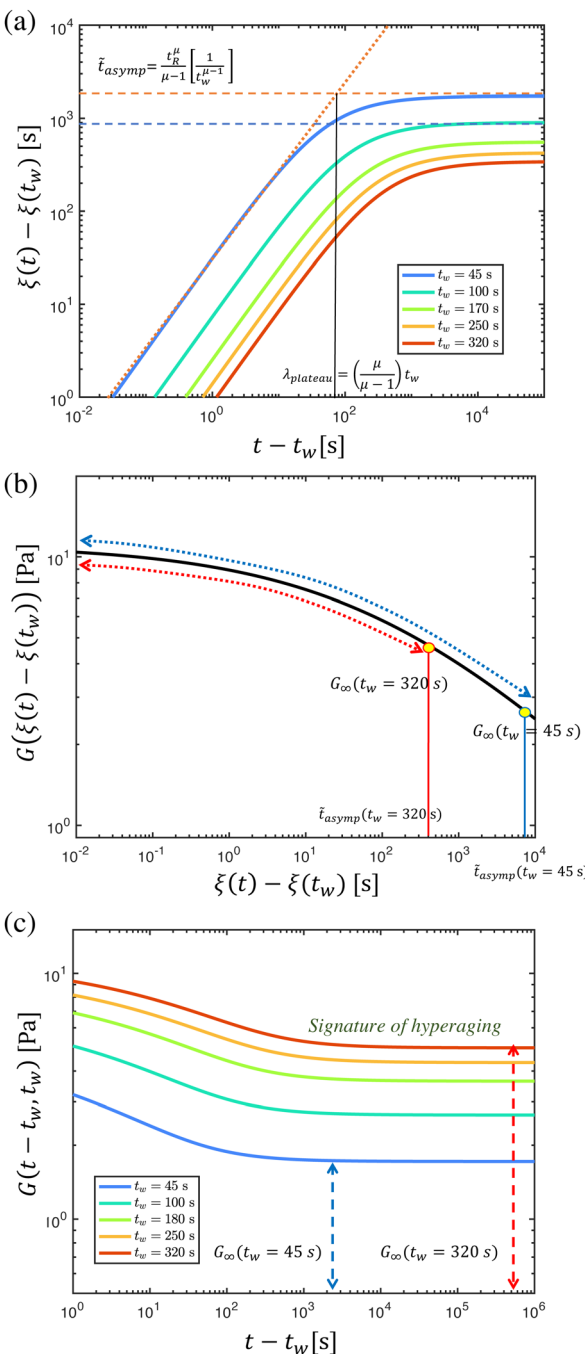


Fig. 12 (a) The dependence of the material time with laboratory time in a hyperaging material for different age times is plotted for $t_R = 400$ s and $\mu = 1.8$. The material time asymptote decreases as the age time increases. (b) The evolution in the relaxation modulus predicted by the fractional Maxwell gel model (FMG) with parameters $\mathbb{G} = 11.1$ Pa, $\mathbb{V} = 51.5$ Pa s 2 , $\alpha = 0.28$ is represented in the material time domain. The aging exponent and reference time in the material time are $\mu = 1.8$ and $t_R = 400$ s respectively. The available information of relaxation modulus in material time for two different times $t_w = 45$ s and $t_w = 320$ s are represented using blue and red solid double headed arrows respectively. (c) The corresponding relaxation modulus in the laboratory time $G(t - t_w, t_w)$ can be evaluated from the relaxation modulus \tilde{G} represented in (b) (in the material time domain using a vertical shift factor form represented by) $b(t_w) = (t_w/t_R)^n$. The complete set of parameters required to construct these curves are $\mathbb{G} = 11.1$ Pa, $\mathbb{V} = 51.5$ Pa s 2 , $\alpha = 0.28$, $\mu = 1.8$, $t_R = 400$ s, $n = -0.36$.

The short-time linear growth of $\tilde{\xi}$ with t given by this equation is evident in Fig. 12(a) and can be used to evaluate an approximate laboratory time (t) at which the asymptotic value of $\tilde{\xi}$ is obtained which we denote by λ_{plateau} :

$$\lambda_{\text{plateau}} = \left(\frac{\mu}{\mu - 1} \right) t_w \quad (30)$$

This relationship is shown graphically in Fig. 12(a) and suggests that the characteristic laboratory time at which structural arrest occurs increases linearly with the wait time. Moreover, we see from any eqn (30) that this relationship is indeed independent of the arbitrarily set reference time t_R .

Therefore, for hyperaging materials subjected to a step deformation after a wait time t_w , the material is only able to access its material-domain relaxation modulus $\tilde{G}(\tilde{\xi})$ in the interval between $0 \leq \tilde{\xi} \leq \tilde{\xi}_{\text{asympt}}(t_w)$. This effect is depicted in Fig. 12(b) for two different wait times, $t_w = 45$ s and $t_w = 320$ s. For laboratory times (wall clock) greater than $t \approx \lambda_{\text{plateau}}$, the material time approaches its plateau value of $\tilde{\xi} = \tilde{\xi}_{\text{asympt}}(t_w)$, with the associated value of the material-domain relaxation modulus $\tilde{G}(\tilde{\xi}_{\text{asympt}}(t_w))$. Therefore, the true relaxation modulus $G(t)$ measured in the laboratory time domain reaches a plateau for times greater than $t \approx \lambda_{\text{plateau}}$ as shown in Fig. 12(c). The value of this plateau can be computed directly from the relaxation modulus in the material domain at $\tilde{\xi}_{\text{asympt}}$ using eqn (12): $G_\infty(t_w) = \tilde{G}(\tilde{\xi}_{\text{asympt}}(t_w))/b(t_w)$.

Fig. 12(c) depicts the resulting plateau in the relaxation modulus for step deformations at different wait times t_w , with the plateau modulus values $G_\infty(t_w) = \tilde{G}(\tilde{\xi}_{\text{asympt}}(t_w))/b(t_w)$, using the empirical form $b(t_w) = (t_w/t_R)^n$ for the vertical shift factor where $t_R = 400$ s and $n = -0.36$.

As a consequence of the structural arrest in the material time coordinate, two signatures can be observed in stress relaxation experiments performed to identify the hyperaging behavior of colloidal gels and glasses:

1. the increase of the asymptotic plateau in the relaxation modulus with wait time t_w , and
2. the linear increase in the laboratory time λ_{plateau} taken to reach this plateau in the relaxation modulus.

Eqn (30) also presents an alternative method for finding the aging exponent μ in hyperaging systems. The traditional method for determining the aging exponent μ in aging systems is by identifying the value of μ that gives the best superposition of relaxation modulus data measured at different values of the waiting time t_w (when accompanied by judicious user-selected choices of the vertical shift factors $b(t_w)$). Instead, one can use eqn (30) to identify the aging exponent μ by experimentally evaluating the laboratory time λ_{plateau} , it takes for the relaxation modulus to reach a plateau as a function of the wait time t_w . Linear regression may then be used to obtain the slope of this relationship, which is equal to $\mu/(\mu - 1)$ according to eqn (30). This method is particularly convenient because it decouples the process of finding the aging exponent μ from the problem of identifying the vertical shift factors $b(t_w)$ that superpose stress relaxation data at different wait times t_w . However, it does

require the modulus of the soft glassy material be large enough to be measured at long times ($t - t_w$) following a small step strain deformation.

Acknowledgements

JDJR was supported by Aramco Americas for his studies into the complex rheology of drilling fluids. K. R. L. was supported by the U.S. Department of Energy Computational Science Graduate Fellowship program under Grant No. DE-SC0020347.

Notes and references

- 1 Advances in Inhibitive Water-Based Drilling Fluids—Can They Replace Oil-Based Muds? 2007, DOI: [10.2118/106476-MS](https://doi.org/10.2118/106476-MS).
- 2 A. A. Anthony, O. C. Esther, D. O. Chris and B. A. Oni, *J. Pet. Explor. Prod. Technol.*, 2020, **10**, 2815–2828.
- 3 M. I. Abdou, A. M. Al-sabagh and M. M. Dardir, *Egypt. J. Pet.*, 2013, **22**, 53–59.
- 4 W. Huang, Y.-K. Leong, T. Chen, P.-I. Au, X. Liu and Z. Qiu, *J. Pet. Sci. Eng.*, 2016, **146**, 561–569.
- 5 B. Erdoçsan and S. Demirci, *Appl. Clay Sci.*, 1996, **10**, 401–410.
- 6 S. Morariu, M. Teodorescu and M. Bercea, *J. Pet. Sci. Eng.*, 2022, **210**, 110015.
- 7 Z. Vryzas, V. C. Kelessidis, L. Nalbantian, V. Zaspalis, D. I. Gerogiorgis and Y. Wubulikasimu, *Appl. Clay Sci.*, 2017, **136**, 26–36.
- 8 S. Bridges and L. Robinson, *A Practical Handbook for Drilling Fluids Processing*, Gulf Professional Publishing, 2020.
- 9 A. Olatunde, M. Usman, O. Olafadehan, T. Adeosun and O. Ufot, *Pet. Coal*, 2012, **54**, 65–75.
- 10 P. Coussot, H. Tabuteau, X. Chateau, L. Tocquer and G. Ovarlez, *J. Rheology*, 2006, **50**, 975–994.
- 11 S. K. Howard, *Formate Brines for Drilling and Completion: State of the Art*, Paper presented at the SPE Annual Technical Conference and Exhibition, Dallas, Texas, October 1995, DOI: [10.2118/30498-MS](https://doi.org/10.2118/30498-MS).
- 12 I. Mukasa-Tebandeke, P. Ssebuwufu, S. Nyanzi, A. Schumann, G. Nyakairu, M. Ntale and F. Lugolobi, *Adv. Mater. Phys. Chem.*, 2015, **05**, 67–86.
- 13 H. J. Skadsem, A. Leulseged and E. Cayeux, *Appl. Rheol.*, 2019, **29**, 1–11.
- 14 J. Mewis and N. J. Wagner, *Adv. Colloid Interface Sci.*, 2009, **147–148**, 214–227.
- 15 R. G. Larson and Y. Wei, *J. Rheol.*, 2019, **63**, 477–501.
- 16 M. Agarwal, S. Sharma, V. Shankar and Y. M. Joshi, *J. Rheol.*, 2021, **65**, 663–680.
- 17 S. M. Fielding, P. Sollich and M. E. Cates, *J. Rheol.*, 2000, **44**, 323–369.
- 18 R. Monicard, *Drilling Mud and Cement Slurry Rheology Manual*, Springer Science + Business Media, 1982.
- 19 P. F. Luckham and S. Rossi, *Adv. Colloid Interface Sci.*, 1999, **82**, 43–92.
- 20 R. E. Grim, *Applied Clay Mineralogy*, McGraw-Hill, 1962.
- 21 H. van Olphen, *J. Colloid Sci.*, 1964, **19**, 313–322.
- 22 V. C. Kelessidis, *Rheology: Open Access*, 2017, **1**, 1000101.
- 23 T. Bhattacharyya, A. R. Jacob, G. Petekidis and Y. M. Joshi, *J. Rheol.*, 2023, **67**, 461–477.
- 24 R. W. Mooney, A. G. Keenan and L. A. Wood, *J. Am. Chem. Soc.*, 1952, **74**, 1367–1371.
- 25 R. Keren, I. Shainberg and E. Klein, *Soil Sci. Soc. Am. J.*, 1988, **52**, 76–80.
- 26 P. Becher, *J. Dispersion Sci. Technol.*, 1988, **9**, 425–426.
- 27 D. M. Marum, M. D. Afonso and B. B. Ochoa, *Appl. Rheol.*, 2020, **30**, 107–118.
- 28 L. J. Michot, I. Bihannic, F. Thomas, B. S. Lartiges, Y. Waldvogel, C. Caillet, J. Thieme, S. S. Funari and P. Levitz, *Langmuir*, 2013, **29**, 3500–3510.
- 29 W. J. Ganley and J. S. Van Duijneveldt, *Langmuir*, 2015, **31**, 4377–4385.
- 30 L. J. Michot, I. Bihannic, K. Porsch, S. Maddi, C. Baravian, J. Mougel and P. Levitz, *Langmuir*, 2004, **20**, 10829–10837.
- 31 R. Greene-Kelly, *Clay Minerals Bulletin*, 1952, **1**, 221–227.
- 32 H. van Olphen, *An Introduction to Clay Colloid Chemistry*, John Wiley & Sons, Ltd, 1963.
- 33 Y. M. Joshi and G. R. K. Reddy, *Phys. Rev. E: Stat., Nonlinear, Soft Matter Phys.*, 2008, **77**, 021501.
- 34 Y. Joshi, *Annu. Rev. Chem. Biomol. Eng.*, 2014, **5**, 181–202.
- 35 Y. M. Joshi, G. K. Reddy, A. L. Kulkarni, N. Kumar and R. P. Chhabra, *Proc. R. Soc. London, Ser. A*, 2008, **464**, 469–489.
- 36 A. Shahin and Y. M. Joshi, *Langmuir*, 2010, **26**, 4219–4225.
- 37 A. Shahin and Y. M. Joshi, *Phys. Rev. Lett.*, 2011, **106**, 038302.
- 38 A. Shukla, S. Shanbhag and Y. M. Joshi, *J. Rheol.*, 2020, **64**, 1197–1207.
- 39 B. Baldewa and Y. M. Joshi, *Polym. Eng. Sci.*, 2011, **51**, 2085–2092.
- 40 R. Gupta, B. Baldewa and Y. M. Joshi, *Soft Matter*, 2012, **8**, 4171–4176.
- 41 M. Kaushal and Y. M. Joshi, *Soft Matter*, 2014, **10**, 1891–1894.
- 42 V. Awasthi and Y. M. Joshi, *Soft Matter*, 2009, **5**, 4991–4996.
- 43 S. Jatav and Y. M. Joshi, *J. Rheol.*, 2014, **58**, 1535–1554.
- 44 R. H. Ewoldt and G. H. McKinley, *Rheol. Acta*, 2017, **56**, 195–210.
- 45 R. R. Fernandes, G. Turezo, D. E. V. Andrade, A. T. Franco and C. O. R. Negrão, *J. Pet. Sci. Eng.*, 2019, **177**, 872–879.
- 46 M.-C. Li, Q. Wu, K. Song, Y. Qing and Y. Wu, *ACS Appl. Mater. Interfaces*, 2015, **7**, 5006–5016.
- 47 M.-C. Li, Q. Wu, T. Lei, C. Mei, X. Xu, S. Lee and J. Gwon, *Energy Fuels*, 2020, **34**, 8206–8215.
- 48 G. Roberts, H. Barnes and P. Carew, *Chem. Eng. Sci.*, 2001, **56**, 5617–5623.
- 49 R. Ran, S. Pradeep, S. Kosgodagan Acharige, B. C. Blackwell, C. Kammer, D. J. Jerolmack and P. E. Arratia, *J. Rheol.*, 2023, **67**, 241–252.
- 50 J. D. John Rathinaraj and G. H. McKinley, *J. Rheol.*, 2023, **67**, 479–497.
- 51 J. D. Martin and Y. T. Hu, *Soft Matter*, 2012, **8**, 6940–6949.



52 T. Divoux, D. Tamarii, C. Barentin and S. Manneville, *Phys. Rev. Lett.*, 2010, **104**, 208301.

53 P. Coussot and G. Ovarlez, *Eur. Phys. J. E: Soft Matter Biol. Phys.*, 2010, **33**, 183–188.

54 S. Sharma, Y. M. Joshi and V. Shankar, *arXiv*, 2023, preprint, arXiv:2302.06129, DOI: [10.48550/arXiv.2302.06129](https://doi.org/10.48550/arXiv.2302.06129).

55 Y. Lin, L. K.-J. Cheah, N. Phan-Thien and B. C. Khoo, *Colloids Surf., A*, 2016, **506**, 1–5.

56 P. Coussot, Q. D. Nguyen, H. T. Huynh and D. Bonn, *J. Rheol.*, 2002, **46**, 573–589.

57 R. H. Ewoldt, C. Clasen, A. E. Hosoi and G. H. McKinley, *Soft Matter*, 2007, **3**, 634–643.

58 R. H. Ewoldt, A. E. Hosoi and G. H. McKinley, *J. Rheol.*, 2008, **52**, 1427–1458.

59 R. H. Ewoldt, A. E. Hosoi and G. H. McKinley, *Integr. Comp. Biol.*, 2009, **49**, 40–50.

60 C. J. Dimitriou, R. H. Ewoldt and G. H. McKinley, *J. Rheol.*, 2013, **57**, 27–70.

61 S. Varchanis, G. Makrigiorgos, P. Moschopoulos, Y. Dimakopoulos and J. Tsamopoulos, *J. Rheol.*, 2019, **63**, 609–639.

62 K. Kamani, G. J. Donley and S. A. Rogers, *Phys. Rev. Lett.*, 2021, **126**, 218002.

63 J. D. J. Rathinaraj, J. Hendricks, G. H. McKinley and C. Clasen, *J. Non-Newtonian Fluid Mech.*, 2022, **301**, 104744.

64 M. Geri, B. Keshavarz, T. Divoux, C. Clasen, D. J. Curtis and G. H. McKinley, *Phys. Rev. X*, 2018, **8**, 041042.

65 E. Ghiringhelli, D. Roux, D. Bleses, H. Galliard and F. Caton, *Rheol. Acta*, 2012, **51**, 413–420.

66 L. C. E. Struik, *Physical Aging in Amorphous Polymers and Other Materials*, Elsevier Science Publishing Company, 1977.

67 A. Shahin and Y. M. Joshi, *Langmuir*, 2012, **28**, 5826–5833.

68 A. Shahin and Y. M. Joshi, *Langmuir*, 2012, **28**, 15674–15686.

69 J. D. J. Rathinaraj, G. H. McKinley and B. Keshavarz, *Fract. Fract.*, 2021, **5**, 174.

70 B. Keshavarz, D. G. Rodrigues, J.-B. Champenois, M. G. Frith, J. Ilavsky, M. Geri, T. Divoux, G. H. McKinley and A. Poulesquen, *Proc. Natl. Acad. Sci. U. S. A.*, 2021, **118**, e2022339118.

71 J. D. J. Rathinaraj, B. Keshavarz and G. H. McKinley, *Phys. Fluids*, 2022, **34**, 033106.

72 K. Lennon, G. McKinley and J. Swan, *Data-Centric Engineering*, 2023, **4**, E13.

73 K. Lennon, J. D. J. Rathinaraj, M. Gonzalez, A. Santra, J. W. Swan and G. H. McKinley, *Rheol. Acta*, 2023, DOI: [10.1007/s00397-023-01407-x](https://doi.org/10.1007/s00397-023-01407-x).